JPRS 78932

9 September 1981

China Report

SCIENCE AND TECHNOLOGY

No. 125

FBIS FOREIGN BROADCAST INFORMATION SERVICE

NOTE

JPRS publications contain information primarily from foreign newspapers, periodicals and books, but also from news agency transmissions and broadcasts. Materials from foreign-language sources are translated; those from English-language sources are transcribed or reprinted, with the original phrasing and other characteristics retained.

Headlines, editorial reports, and material enclosed in brackets [] are supplied by JPRS. Processing indicators such as [Text] or [Excerpt] in the first line of each item, or following the last line of a brief, indicate how the original information was processed. Where no processing indicator is given, the information was summarized or extracted.

Unfamiliar names rendered phonetically or transliterated are enclosed in parentheses. Words or names preceded by a question mark and enclosed in parentheses were not clear in the original but have been supplied as appropriate in context. Other unattributed parenthetical notes within the body of an item originate with the source. Times within items are as given by source.

The contents of this publication in no way represent the policies, views or attitudes of the U.S. Government.

PROCUREMENT OF PUBLICATIONS

JPRS publications may be ordered from the National Technical Information Service, Springfield, Virginia 22161. In ordering, it is recommended that the JPRS number, title, date and author, if applicable, of publication be cited.

Current JPRS publications are announced in Government Reports Announcements issued semi-monthly by the National Technical Information Service, and are listed in the Monthly Catalog of U.S. Government Publications issued by the Superintendent of Documents, U.S. Government Printing Office, Washington, D.C. 20402.

Indexes to this report (by keyword, author, personal names, title and series) are available from Bell & Howell, Old Mansfield Road, Wooster, Ohio 44691.

Correspondence pertaining to matters other than procurement may be addressed to Joint Publications Research Service, 1000 North Glebe Road, Arlington, Virginia 22201.

JPRS 78932

9 September 1981

CHINA REPORT

SCIENCE AND TECHNOLOGY

No. 125

CONTENTS

PEOPLE'S REPUBLIC OF CHINA

APPLIED SCIENCES

PUBLICATIONS

ABSTRACTS

THEORETICAL ANALYSIS OF EFFECT OF LANGMUIR FLOW IN RING LASER

Shanghai JIGUANG [LASER JOURNAL] in Chinese Vol 8 No 4, Apr 81 pp 1-8

[Article by Jiang Yanan [1203 0068 0589] of the Department of Precision Instruments of Qinghua University: "Theoretical Analysis of the Effect of Langmuir Flow in a Ring Laser." This article was received on 12 March 1980]

[Text] Abstract: The flow of gas in a gain medium is an important source of error in laser gyros. This article quantitatively discusses the drift of the frequency difference of opposite carrier waves brought about by the flow of active and non-active atoms in the gain medium. The article gives the theoretical formula and the computed values of Langmuir flow in the third order theory. This article emphasizes the use of statistical methods to treat the drift of frequency difference when a Gaussian beam passes through the gain field and the flow velocity field. It also gives the computational formulas for various conditions.

I. Introduction

In a ring-shaped laser, traveling wave oscillations in the clockwise and counterclockwise directions of propagation are maintained. Because the activeness of the gaseous gain medium is sustained by direct current discharge, unavoidably, this will cause gases to flow inside the discharge tube. In the He-Ne ring laser of small power, the typical value of the flow velocity is about several centimeters/second. This type of flow is called Langmuir flow. It will result in a split in frequency of the traveling waves in the clockwise and the counterclockwise directions. Its typical value $\Delta\nu_L$ is about several dozen hertz.

Everyone knows that when the ring laser undergoes a rotation Ω relative to the inertial space, because of the effects of relativity theory, a frequency difference will be produced between the clockwise and the counterclockwise traveling waves:

$$\Delta\nu_\Omega = |\nu^{cw} - \nu^{ccw}| = \frac{4S\cdot\Omega}{\lambda L} \qquad (1)$$

where S is the area enveloped by the ring cavity, L is the length of the cavity of the ring, λ is the wavelength of the laser.

$K = \frac{4S}{\lambda L}$ is called the graduation factor of the gyro. To define a quantitative concept, the typical value of K in an actual laser gyro is about 1 hertz/degree/hour. Therefore, to obtain a sensitivity above 10^{-2} degrees/hour, all sources of error which can cause a drift in the frequency difference $\Delta\nu$ between the clockwise and the counterclockwise traveling waves must be stabilized at below 10^{-2} hertz.

We have already mentioned above that the typical value of Langmuir flow is $\Delta\nu_L$ several dozen hertz. The seriousness of the error source causing a zero drift of the laser gyro can thus be seen.

For this, in an actual laser gyro, a double anode discharge tube is used (See Figure 1).

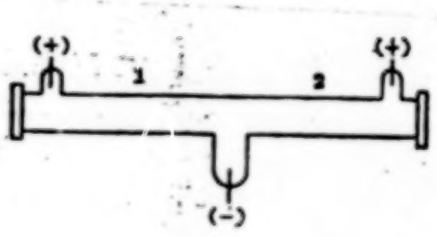

Figure 1. Dual circuit discharge tube 1, 2

Even so, because of the complexity and the instability of interaction among the Gaussian beam, the Langmuir flow velocity field and the gain field, significant constant drift and random drift will be brought about. In particular, in the four-frequency differential laser gyro, the result of differential motion is the elimination of some major error sources, but the drift caused by Langmuir flow will multiply. Therefore, in a high precision gyro, the study of the effects of Langmuir flow is very important.

In a He-Ne gaseous gain tube of direct current discharge, the so-called flow of gaseous atoms includes two types, the flow of active atoms (Ne*) and of nonactive atoms (such as He and nonactive Ne). Their directional flow will all cause the non-mutually countering effect described above--causing a frequency difference between the clockwise and counterclockwise traveling waves to occur--i.e., zero drift. But the physical mechanisms of zero drift caused by the nonactive atoms and the gain atoms are different, therefore they must be separately discussed.

The Langmuir flow effects of nonactive atoms are relatively simple. According to the effect of Fresnel traction of the velocity of light in the moving medium, the term of Langmuir drift in the nonactive medium is

$$\Delta\nu'_L = -\frac{4S}{\lambda L}\left(1-\frac{1}{n^2}\right)\bar{\Omega}' \qquad (2)$$

where $\bar{\Omega}'$ is the equivalent angular velocity of the nonactive medium relative to the motion of the ring cavity.

Calculations show that under ordinary conditions, this term is smaller than the Langmuir drift in an active medium by three magnitudes. This article will emphasize the discussion of Langmuir flow effects of active atoms.

II. Basic Equations

Refer to references (1 - 3). The circular frequencies (ω_1 , ω_2) of the opposite traveling waves in the ring laser satisfy the following equations respectively

$$\omega_1 = \Omega_1 + \sigma_1 + \rho_1 I_1 + \tau_{12} I_2 \tag{3}$$

$$\omega_2 = \Omega_2 + \sigma_2 + \rho_2 I_2 + \tau_{21} I_1 \tag{4}$$

This is the result of the third order theory for the intensity of electrical polarization of an active medium. The formulas have omitted the corresponding terms related to locking because the questions discussed in this article are unrelated to locking, and they also signify that the ring laser should be operated at a point far away from the locked area. The formulas are completely satisfied by the four-frequency device used in this article. In the formulas, 1, 2 respectively represent the clockwise and the counterclockwise traveling waves. $\Omega_{1,2}$ is the harmonic oscillation of the empty cavity. σ is the chromatic dispersion coefficient of the active medium. ρ and τ are the gain saturation parameters of the medium.

From (3) and (4) we can obtain the circular frequency difference between the clockwise and the counterclockwise traveling waves

$$\begin{aligned}\omega = \Omega &+ (\sigma_2 - \sigma_1) + (\tau_{21} - \rho_1) I \\ &- (\tau_{12} - \rho_2) I_2\end{aligned} \tag{5}$$

where $\Omega = \Omega_2 - \Omega_1$ is the circular frequency difference of the empty cavity.

When considering the effects of radiation trapping and when using the average light intensity I and the light intensity difference i

$$I = \frac{1}{2}(I_2 + I_1) \tag{6}$$

$$i = \frac{1}{2}(I_2 - I_1) \tag{7}$$

we obtain

$$\begin{aligned}\omega = \Omega &+ (\sigma_2 - \sigma_1) + 2(\rho - \tau) i \\ &- \left[\frac{2R}{G}(\sigma_2 \beta_2 - \sigma_1 \beta_1)\right. \\ &\left. + (\tau_{12} - \tau_{21}) + (\rho_1 - \rho_2)\right] I\end{aligned} \tag{8}$$

Deleting the term of light intensity difference, i.e., letting i = 0, and using the frequency parameter

$$\xi_i = \frac{\omega_i - \omega_0}{Ku} \quad i = 1, 2$$

equation (8) can be expressed as

$$\omega = \Omega(1 + A) \tag{9}$$

$$A = \frac{G}{2Ku}\left(\frac{C}{L}\right)[S_\sigma + S_R + S_\tau + S_\rho] \tag{10}$$

A in equation (9) shows the existence of an active medium, it is a readjustment of the frequency difference of the empty cavity, called the ratio factor correction term. In equation (10), S_σ , S_R , S_τ , S_ρ respectively represent the difference correction terms of mode traction, radiation trapping, and self and mutual repulsion of modes.

Let

$$S = S_\sigma + S_R + S_\tau + S_\rho \tag{11}$$

These parameters can be written as the following under the condition where the double isotope Ne^{20} :Ne^{22} =1:1

$$S_\sigma = -\frac{\frac{1}{2}[Z_1' + Z_2']}{Z_{1m}}$$

$$S_R = -\frac{\left\{-\frac{1}{2}\eta I[(Z_1' + Z_2')(b + b') + (Z_1 + Z_2)(b' + b')]\right\}}{Z_{1m}}$$

$$S_\tau = -\frac{-\frac{1}{2}\eta I\left[\frac{Z_1'}{\xi} + \frac{Z_1'}{(\xi - \xi_t)}\right]}{Z_{1m}}$$

$$S_\rho = -\frac{-\frac{1}{2}\eta I[Z_1' + Z_2']}{Z_{1m}}$$

where $b=(Z_i - \eta Z_r')/Z_{im}$, Z_i and Z_r represent the imaginary and the real parts of the chromatic dispersion function of the plasma. ξ_t is the frequency pitch of the two types of isotopes. $Z_{im} = Z_i(0)$ is the maximum value of this function. Calculations show: S_σ and S_R are larger than S_τ , S_ρ by one magnitude[3].

III. General Description of the Langmuir Flow Effect

In the discharge tube of the ring laser, because of direct current discharge, the gain atoms have a definite flow velocity V. Because of the Doppler effect, the

gain curves of the traveling waves 1 and 2 produce a 2KV circular frequency split. Thus, the frequency difference formula of the gyro becomes

$$\omega = \Omega(1 + A) - 2KV \cdot A \tag{12}$$

This shows that the circular frequency difference term of the Langmuir flow is:

$$\Delta\omega = -2KV A$$

This is because the split in the gain curves of the clockwise and the counterclockwise light has led to the introduction of different values in the gain medium due to the effects of traction and repulsion of the clockwise and counterclockwise light.

In the four-frequency differential laser, because of the simulataneous rotation of the left and right rotary gyro, added to the output signal of the left and right rotary differential

$$\Delta\omega = \omega_{left} - \omega_{right}$$

is

$$\Delta\omega = 4KV \cdot \bar{A} \tag{13}$$

This is the circular frequency drift term of the Langmuir flow effect in the four-frequency differential laser gyro, and in the equation

$$\bar{A} = \frac{1}{2}(A_{left} + A_{right}) \tag{14}$$

Figure 2 illustrates the working principles of the four-frequency differential gyro. The 90° quartz optical rotator causes the frequency pitch of the left and right rotary gyro to be $\frac{C}{2L}$ (half of the mode pitch). The cavity frequency controler and the piezoelectric components make sure that the left and right gyro works on symmetric operating points on the gain curves. To avoid competition between modes and symmetry of the gain curves, the devices are filled with an equal proportion of Ne^{20} and Ne^{22}. The photomagnetic Faraday component produces equal operating points of opposite partial frequency for the left and right gyros to avoid the lock area.

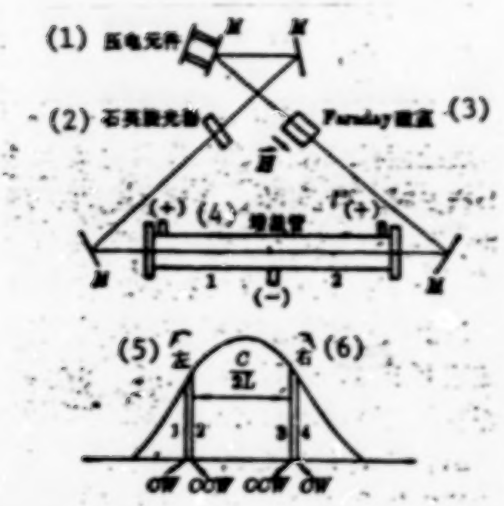

Figure 2. Simple illustration of the operating principle of the four-frequency gyro (N is the angular reflector)

Key:

1. Piezoelectric component
2. Quartz optical rotator
3. Faraday magnetic chamber
4. Gain tube
5. Left
6. Right

Here we combine the parameters of the four-frequency device of the experiment to give a set of estimated values of Langmuir flow.

Let the effective value of the directional flow velocity of the gain atoms in the discharge tube be V = 1 centimeter/second, then, the frequency split of the gain curve is

$$\frac{KV}{\pi} = 0.0317 \text{ megahertz},$$

the Langmuir flow frequency drift introduced here is

$$\Delta\nu_L = -\frac{4V}{\lambda}\bar{A} \tag{15}$$

$$\bar{A} = -\frac{C}{2L}\frac{G}{Ku}S \tag{16}$$

This device has a length of L = 63.3 centimeters, thus

$$\frac{C}{2L} = 241 \text{ megahertz}.$$

He-Ne filling pressure is P = 3.3 torr, thus η = 0.2; bandwidth of the emitted light is $\Delta\xi$ = 0.4, thus the gain/loss ratio is G/r = 1.17. Because r = 3%, we have G = 3.51%. Therefore

$$\frac{C}{2L}\frac{G}{Ku} = 1.84\times10^{-4},$$

$$\bar{\lambda} = 0.968\times10^{-4},$$

$$\Delta\nu_L = 61.1 \text{ hertz.}$$

In the dual anode discharge tube, the gain and the flow velocity of atoms of the discharge tube of two sections are respectively denoted as G_1, G_2, V_1, V_2. Thus

$$\Delta\nu_L = \frac{4(G_2V_2 - G_1V_1)}{\lambda G}\bar{I}^m \tag{17}$$

Let $$G_1 = G_2 = \frac{1}{2}G,$$

$$\Delta\nu_L = 2\frac{V_2 - V_1}{\lambda}\bar{I}.$$

When $V_2 - V_1 = 1$ centimeter/second, $\Delta\nu_L \approx 30.6$ hertz.

Measurements of the experiment show that when the electric current differential between the two segments of the discharge tube is $\Delta I = 1$ milliamperes, $\Delta\nu_L = 52$ hertz. This shows that at this time, the differential value of the flow velocity of the two segments of the discharge tube is

$$V_2 - V_1 = 1.7 \text{ centimeters/second.}$$

In the above, we started out from the directional flow velocity V of the gain atoms present in the discharge tube and discussed in general the cause of the Langmuir flow drift and numerical estimation.

$\Delta\nu_L$ and G, V are directly proportional, but generally speaking, the G, V in the gaseous discharge tube are not constant. They are distributed radially and axially according to a definite pattern. Therefore, to further discuss the zero drift of Langmuir flow, we will analyze the gain coefficient and the field distribution of the flow velocity.

IV. Lateral Distribution of the Velocity and the Gain Coefficient Fields

(1) Flow Velocity Field

In the positive cylindrical region of the closed direct current He-Ne discharge tube there exist two types of opposite flow of gaseous atoms. One type is the Langmuir flow, its direction is from the negative pole to the positive pole, it is due to the negative charge effect of the wall of the discharge tube. When the free range of the ions $\lambda_+ \ll$ a (radius of the discharge tube), the velocity distribution in the direction r along the radius of the capillar tube is

$$V_L(r) = V_L(0)\left[1 - e^{-\frac{r}{\lambda_+}}\right]^m \tag{18}$$

In the 3 torr He:Ne=7:1 discharge tube, $\lambda_+ \sim 0.05$ millimeters.

The result of Langmuir flow causes an atmospheric pressure difference between the positive and the negative poles of the closed discharge tube. Under the effect of the pressure difference, a second type of flow is formed in the discharge tube: a viscous flow (Poiseuille flow) $V_p(r)$ from the positive pole to the negative pole, its distribution is

$$V_p(r) = V_p(0)\left[1-\left(\frac{r}{a}\right)^2\right] \tag{19}$$

In a closed discharge tube, a stable flow is formed under an equilibrium condition, thus

$$\int_0^{2\pi}\int_0^a V_p(r)\, r\, dr\, d\theta = \int_0^{2\pi}\int_0^a V_L(r)\, r\, dr\, d\theta$$

Let $a = 0.75$ millimeters, then $a/\lambda_+ \approx 15$, we have

$$V_L(0) \approx \frac{4}{7} V_p(0).$$

The flow velocity V(r) of the gaseous atoms is a combination of the two opposite flows described above, i.e.

$$\begin{aligned} V(r) &= V_p(r) - V_L(r) \\ &= V_0\left[1-\frac{7}{8}\left(\frac{r}{a}\right)^2+\frac{4}{8}e^{\frac{r^2-a^2}{\lambda_+ a}}\right] \end{aligned} \tag{20}$$

We know from equation (20) that when

$$\begin{cases} r = a \\ r = 0.65a \end{cases} \qquad V(r) = 0$$

and in the region $r < 0.6$ millimeters, the above equation simplifies to

$$V(r) = V_0\left[1-\frac{7}{8}\left(\frac{r}{a}\right)^2\right] \tag{21}$$

Equation (2) can be used for the flow velocity in the region passed through by the Gaussian beam discussed in this article.

Figure 3 gives the flow velocity diagram obtained from equation (20). It can be seen from the diagram that in the central area of the discharge tube, atoms flow from the positive pole to the negative pole. In the border regions of the discharge tube, atoms flow from the negative pole to the positive pole. In the cross section, the total flow towards the positive and the negative poles are equal[5].

But it should be pointed out that the actual flow velocity field is more complex than this and should be further studied.

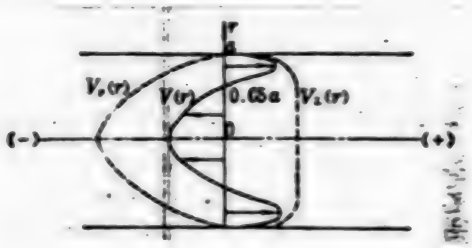

Figure 3. Lateral distribution of the flow velocity in the discharge tube V(r)

(2) The Field of Gain Coefficients

The distribution of the gain coefficients determined by the distribution of the electron density n_e in the discharge tube (Figure 4) is

$$G(r) = G_0 J_0\left(\frac{2.4r}{a}\right) \tag{22}$$

while the one-way gain coefficient generally defined should be the average value of G(r) in the region passed through by the Gaussian beam.

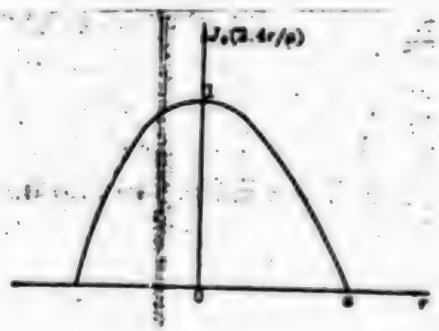

Figure 4. Lateral distribution of the gain field in the discharge tube $G(r) = G_0 J_0 (r)$

V. Zero Drift of Langmuir Flow Under an Eccentric Guassian Beam

We discussed above the lateral distribution of the gain coefficient G(r) and the flow velocity V(r) along the discharge tube. The problem facing this article is the zero drift $\Delta\nu_L$ of the "Langmuir" flow created when the Gaussian beam of an intensity distribution (e^{-r^2/a^2}) passes through the gain field and the flow velocity field at eccentricity a in the discharge tube.

Because G, V are functions of r, $\Delta\nu_L$ must also be a function of r. Thus, the Langmuir zero drift that exerts an effect in the experiment should be directly proportional to the statistical average value of $G(r) \cdot V(r)$ with e^{-r^2/a^2} as the weighting factor.

From equations (15) and (16)

$$\Delta\nu_L = QGV \tag{23}$$

where

$$Q = \bar{A}\frac{4}{\lambda\bar{G}} \tag{24}$$

Because the Gaussian beam and the G, V fields have an eccentricity α, we select the origin O of the cylindrical coordinates (r, θ) to coincide with the center of the Gaussian beam, thus the gain field and the flow velocity field having the center of the discharge tube O' in these coordinates as the center of symmetry are respectively G(r'), V(r'), while $\overline{OO'} = \bar{\alpha}$. See Figure 5.

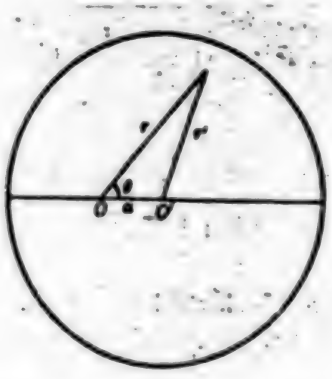

Figure 5. The center of the Gaussian beam deviates from the center O' of the discharge tube, the deviation is α

$$(r')^2 = r^2 + a^2 - 2ra\cos\theta$$

$$\langle\Delta\nu_L\rangle_0 = -Q\langle G\cdot V\rangle_0$$

$$= -Q\frac{\int_0^{2\pi}\int_0^{\infty} e^{-r^2/w^2} G_0 J_0(2.4r'/a) V(r') r\,dr\,d\theta}{\int_0^{2\pi}\int_0^{\infty} e^{-r^2/w^2} r\,dr\,d\theta} \tag{25}$$

From this we can calculate

$$\langle\Delta\nu_L\rangle_0 = -QG_0V_0\left[0.6951 - 2.735\left(\frac{a}{a}\right)^2 + 3.87\left(\frac{a}{a}\right)^4\right]$$

$$= -QG_0V_0 f(a) \tag{26}$$

Retaining the second order terms, we have

$$f(a) = 0.6951 - 2.735\left(\frac{a}{a}\right)^2 \tag{27}$$

In a closed dual anode discharge tube

$$\langle \Delta \nu_L \rangle_\alpha = Q[G_{10} V_{10} f(\alpha_1) - G_{20} V_{20} f(\alpha_2)] \tag{28}$$

where G_{10}, G_{20} and V_{10}, V_{20} are respectively the gain coefficient and flow velocity at the centers of the two segments 1 and 2 of the discharge tube respectively. See Figure 2.

$G_0 = G_{10} + G_{20}$, let the two segments of the discharge tube be centered, i.e., $\alpha_1 = \alpha_2 = \alpha$, then

$$\langle \Delta \nu_L \rangle_\alpha = Q[G_{10} V_{10} - G_{20} V_{20}] f(\alpha) \tag{29}$$

Obviously, when $G_{10}\, V_{10} = G_{20}\, V_{20}$, $\langle \Delta \nu_L \rangle_\alpha = 0$, i.e., the zero drift of Langmuir flow is zero. But when

$$G_{10} = G_{20} = \frac{G_0}{2}$$

$$\langle \Delta \nu_L \rangle_\alpha = Q G_0 \left(\frac{V_{10} - V_{20}}{2} \right) f(\alpha) \tag{30}$$

VI. Relative Systematic Zero Drift γ_α and Random Zero Drift β_α

This article is concerned about the added zero drift introduced by the eccentricity α of the base mode of oscillation in the ring cavity relative to the discharge tube because of initial maladjustment and the random change of zero drift introduced by the continuous change ($\Delta\alpha$) of α due to such factors as instability of the cavity in the experimental process.

To describe the relative change of this type of zero drift, two parameters γ_α, β_α are introduced. They are defined as

$$\gamma_\alpha \equiv \frac{\langle \Delta \nu_L \rangle_\alpha - \langle \Delta \nu_L \rangle_{\alpha=0}}{\langle \Delta \nu_L \rangle_{\alpha=0}} = -8.935 \left(\frac{\alpha}{a} \right)^2 \tag{31}$$

$$\beta_\alpha \equiv \frac{\frac{d \langle \Delta \nu_L \rangle_{\alpha+\Delta\alpha/2}}{d\alpha} \cdot \Delta\alpha}{\langle \Delta \nu_L \rangle_\alpha} = -\frac{8.935(2\alpha + \Delta\alpha)\Delta\alpha}{a^2} \tag{32}$$

Let a = 0.75 millimeters, we have Table 1.

Table 1. The relative variation γ_α of the zero drift of Langmuir flow when the Gaussian beam deviates from the center α of the gain tube

α (millimeter)	γ_α
0.01	-7.0×10^{-4}
0.075	-3.9×10^{-2}
0.1	-7.0×10^{-2}
0.2	-0.25

Let a = 0.75 millimeter, α = 0.1 millimeter, we have Table 2.

Table 2. Relative variation β_α of the zero drift of the Langmuir flow introduced by the random variation $\Delta\alpha$ of α when the Gaussian beam deviates from the gain tube center by α = 0.1 millimeter.

$\Delta\alpha$ (millimeter)	β_α
0.001	-1.4×10^{-3}
0.01	-1.47×10^{-2}
0.02	-3.08×10^{-2}
0.03	-4.83×10^{-2}
0.05	-8.75×10^{-2}

It can be seen from the above that readjustment of the ring cavity should make the deviation α as small as possible, thus under an equal amount of random deviation $\Delta\alpha$, the random variation of the zero drift of the Langmuir flow becomes small.

VII. Zero Drift of Langmuir Flow When the Gaussian Beam Passes Through Obliquely[7]

In an actual ring cavity, the Gaussian beam also passes through the discharge tube obliquely. At this time, on the central z axis of the oblique Gaussian beam, the distribution of G, V at different z is different. This is equivalent to the presence of a different deviation $\alpha(z)$ at different z. See Figure 6.

Figure 6. Drift of Langmuir flow when the Gaussian beam (along the z axis) passes through the gain tube obliquely

To further explain this problem, we must discuss the distribution of the gain and flow velocity along the z axis.

The one-way gain coefficient G used in previous discussions necessarily neglects the distribution of gain along the z axis. Here we introduce the gain density g, i.e., the concept of the gain value in a unit length. In cylindrical coordinates, it is $g(r, \theta, z)$, and

$$G(r\theta)=\int_0^{l_0} g(r,\ \theta,\ z)\,dz_0$$

The relationship between g (r, θ, z) and $\overline{G}$ is

$$\overline{G}=\frac{\int_0^{l_0}\int_0^{2\pi}\int_0^{r_m} g\,(r,\ \theta,\ z)\,r\,dr\,d\theta\,dz}{\int_0^{2\pi}\int_0^{r_m} r\,dr\,d\theta} \tag{33}$$

$0 \rightarrow l_0$ is the length of the gain region.

The above equation shows that the one-way gain $\overline{G}$ is the radial average of the gain density in the effective zone of the Gaussian beam and the axial cumulative value. Obviously, when the Gaussian beam moves inside the discharge tube, the one-way gain $\overline{G}$ provided to it by the gain tube will also change.

The Langmuir zero drift when the Gaussian beam passes through the discharge tube obliquely is written as $\langle \Delta\nu_L\rangle_{a(z)}$, $a(z)$ is the deviation of the center of the Gaussian beam at z from the center of the tube.

$$\langle \Delta\nu_L\rangle_{a(z)}=\frac{\left\{Q\int_0^{l_0}\left[\int_0^{2\pi}\int_0^{r_m} e^{-r'/r_m} g(r',\ z)\right.\right.}{\left.\left.\times V(r',\ z)\,r\,dr\,d\theta\right]dz\right\}}$$
$$\int_0^{2\pi}\int_0^{r_m} e^{-r'/r_m} r\,dr\,d\theta$$
$$-Q\int_0^{l_0} k_0 V_0 f[a(z)]\,dz \tag{34}$$

In the dual anode discharge tube, let the lengths of the two segments of the discharge tube be the same, then

$$\langle \Delta\nu_L\rangle_{a(z)}=-Q\left\{G_{10}V_{10}\frac{\int_0^{\frac{l_0}{2}} f[a_1(z)]\,dz}{\frac{l_0}{2}}\right.$$
$$\left.-G_{20}V_{20}\frac{\int_{\frac{l_0}{2}}^{l_0} f[a_2(z)]\,dz}{\frac{l_0}{2}}\right\} \tag{35}$$

where $G_{10}=g_{10}\frac{l_0}{2}$ $G_{20}=g_{20}\frac{l_0}{2}$.

In the following, we will progress further to give the actual form of $a(z)$ to complete integration. Let the central axis z of the Gaussian beam and the central axis z' of the discharge tube intersect in space at the point of intersection 1', the angle of intersection is ψ . Then, $a_1(z)$, $a_2(z)$ can use the uniform expression

$$\alpha(z) = (z - 1')\tan\psi \tag{36}$$

$\alpha(z)$ has $1'$ and ψ as its parametric variables, thus the $\langle \Delta\nu_L \rangle_{\alpha(z)}$ above can be rewritten as $\langle \Delta\nu_L \rangle_{V,\psi}$ for more clarity.

Also, let $G_{20} = G_{10} = \frac{1}{2} G_0$, $V_{10} = V_{20} = V_0$,

then

$$\langle \Delta\nu_L \rangle_{V,\varphi} = \frac{2.735 \times Q G_0 V_0 l_0}{a^3} \times \left(\frac{1}{2} - \frac{l'}{l_0}\right)\tan^2\varphi \tag{37}$$

The relative variations β_ψ, $\beta_{1'}$ introduced by $\langle \Delta\nu_L \rangle_{V,\psi}$ when ψ or $1'$ changes (due to a change in the shape of the cavity are defined as

$$\beta_\psi = \frac{\frac{d\langle \Delta\nu_L \rangle_{V,\varphi}}{d\varphi} \cdot \Delta\varphi}{\langle \Delta\nu_L \rangle_0} \tag{38}$$

Calculations yield

$$\beta_\psi = -7.86\left(\frac{l_0}{a}\right)^2\left(\frac{1}{2} - \frac{l'}{l_0}\right)\tan\varphi \cdot \Delta\varphi \tag{39}$$

$$\beta_{l'} = \frac{\frac{d\langle \Delta\nu_L \rangle_{V,\varphi}}{dl'} \cdot \Delta l'}{\langle \Delta\nu_L \rangle_0} \tag{40}$$

Calculations yield

$$\beta_{l'} = -3.93(\tan^2\varphi) \cdot \frac{l_0}{a^3} \Delta l' \tag{41}$$

Let the length of the gain region of the discharge tube l_0 = 200 centimeters, a = 0.75 millimeters, then

a) β_ψ, let $1' = \frac{1}{4} l_0$, $\psi = 2'$, listed in Table 3.

Table 3. Relative variation β_ψ of the zero drift of Langmuir flow introduced by the changes in inclination ψ when the Gaussian beam passes obliquely through the gain tube.

$\Delta\psi$	β_ψ
10"	3.5×10^{-3}
1'	2.1×10^{-2}
2'	3.5×10^{-2}

b) $\beta_{1'}$ let $\psi = 2'$, listed in Table 4.

Table 4. Relative variation $\bar{\beta}_{1'}$ of the zero drift of Langmuir flow introduced by the variation in the point of intersection 1' when the Gaussian beam passes obliquely through the gain tube

$\Delta 1'$ (millimeter)	$\bar{\beta}_{1'}$
1	-3.5×10^{-4}
10	-3.5×10^{-3}

The β_α, $\bar{\beta}_{1'}$, β_ψ, given above respectively represent the relative variation of the zero drift of Langmuir flow introduced when the central axis z of the Gaussian beam translates or inclines towards the central axis z' of the discharge tube. But under ordinary conditions, z and z' are spatially nonintersecting. We can prove that the shortest distance between z and z' must be perpendicular to z, z'. Let z be translated along the direction of this perpendicular line to the shortest distance a_0, it will then intersect the z' axis at 1', with an angle of intersection ψ. Then,

$$a^2(z) = a_0^2 + (z - 1')^2 \tan^2 \varphi$$

$f(a) = 0.6951$

$$-\frac{2.735}{a^3}\left[a_0^2 + (z - 1')^2 \tan^2 \varphi\right]$$

It can be seen under this situation

$$\beta = \beta_\alpha + \beta_{1'} + \beta_\psi \tag{42}$$

where β_α, $\bar{\beta}_{1'}$, β_ψ are respectively according to equations (32), (41), (39). They will not be discussed here again.

This article was presented during the course of developing the "four-frequency differential laser gyro" prototype jointly by Qinghua University, the State Measurement Sciences Academy, the Suzhou First Optical Instruments Plant. Colleagues such as Feng Tiesun [7458 6993 5549], Liu Weimin [0491 5898 3046], and Bao Chengyu [0545 2052 3768] provided assistance. The comrades of the Measurement Academy also conducted the corresponding experimental research, we thank them here.

References

(1) Gao Bolong [7559 0130 7893], "Ring Laser Lecture Notes".

(2) Aronowitz F., Appl. Opt., 1972, 11, 2146.

(3) Aronowitz F. et al., IEEE J. Quant. Electr., 1974, QE-10, 201.

(4) Podgorski, T. L., Aronowitz F., IEEE, J. Quant. Electr., 1968, QE-4, 4.

(5) Druyvestey M. J., Physica., 1935, 2, port 1, 255-266.

(6) Shimagai Kanfu, Tominaga Itsuro, "Vacuum Physics and Application", 1971.

(7) Liao Fuzhong [1675 1788 0022], "Laser", 1979, 6, No 12, 1.

9296
CSO: 4008/421

ANALYTICAL DESCRIPTION OF TIME CHARACTERISTICS OF HIGH POWER LASER PULSES

Shanghai JIGUANG [LASER JOURNAL] in Chinese Vol 8 No 4, Apr 81 pp 9-13

[Article by Yang Hanqian [2799 3211 0241] and Qu Zhimin [2575 1807 2404] of the Shanghai Laser Technology Institute and Liu Songhao [0491 7313 6275] and He Guangsheng [6378 0342 3932] of the Shanghai Optics and Fine Mechanics Institute of the Chinese Academy of Sciences: "Analytical Description of the Time Characteristics of High Power Laser Pulses." This article was received on 14 May 1980]

[Text] Abstract This article expands the studies by Wagner and Lengyel[1], obtains the solution of the time parameters of high power laser pulses, gives the mathematical relationship of the time a pulse is established, and brings out the effects of the section of the active medium upon the time a pulse is established, the single pulse condition and the pulse width.

The time parameters of high power laser pulses are the major variables[1] that describe the variation of each physical quantity in time during the course of laser oscillations. The time of establishment of a pulse T_r is also an important physical quantity[2,3]. In the past, several methods of estimation[3,4] were used to determine T_r, while ordinarily, only the numerical solution[1,5] by the computer is given. Articles of recent years have described various methods to analytically describe the process[6,7] of establishment of a light pulse. This article has used different methods to sum up the problem into one seeking a solution for the time parameter and more precise results have been obtained. The method of derivation in this article and the results are suitable for analysis of the single pulse in the relaxation oscillation process.

I. Solution of the Time Characteristic in the Oscillation Process

1. Solution of the Time Parameter

To describe the process of the establishment of a pulse, reference (1) divides the pulse into three zones, zone A, zone B and zone C. In zone B, the form of the solution of the time parameter of the pulse is

$$t' = \int_{s_1}^{s} \frac{ds}{F(s)}. \tag{1}$$

The function to be integrated is

$$F(z) = e^{-z} - e^{-z_1} + z_1 - z_0 \tag{2}$$

See reference (1) for an explanation of the symbols.

At first glance, the integration of the above equation does not seem to be complicated, but seen from the point of view of calculus, it is impossible to obtain the analytic form of the original function. Reference (1) uses the numerical solution obtained by the computer. To seek the mathematical relationship among the physical quantities, it is best to obtain the approximate analytic solution of the time parameter. We first substitute the variables of the function to be integrated and take

$$x = -\ln \frac{n}{n_1} \tag{3}$$

thus we obtain the relationship between x and z

$$x = z + x_p, \; x_p = -z_1,$$

and

$$x_1 = 0.01, \; x_2 = x_f - 0.01.$$

After substitution of variables, the form of the solution of the time parameter in zone B ($x_1 < x < x_2$) is

$$t' = \int_a^z \frac{dz}{F(z)}. \tag{4}$$

The function to be integrated is

$$F(z) = \frac{1}{n_0}[n_1 - a_1 z - a_2 \exp(-z + z_p)] \tag{5}$$

In equation (5), the physical meaning of the exponential term is very clear, it represents a physical parameter of the system--the inverse density n of the number of particles. We expand the exponential term by its power. This expansion signifies the expansion of the values of the inverse density n of the number of particles in an undisturbed stable state, then we retain the first three terms to obtain the second degree approximate analytic solution.

The approximate analytic expression of the time parameter in zone B obtained by computation is

$$t' - t_0 = -\frac{1}{b} \ln \left| \frac{(z - z_p) - b}{(z - z_p) + b} \right|, \tag{6}$$

where the factor

$$b = \left[2\left(a + \ln \frac{n_2}{n_1}\right)\right]^{1/2}$$

and the factor

$$a = \frac{n_1}{n_0} - 1.$$

2. Solution of the Time of Establishing the Pulse

Now we define the time of establishing a pulse after the switch is turned on as the period when the density of the number of photons start out from an initial value ψ_i to the moment it reaches its peak value ψ_p

$$T_r - T_1 - t_1 = \frac{1}{a}\ln\left(1+\frac{n_1-n_2}{200\varphi_1}\right) + \frac{1}{b}\ln\left|\frac{(0.01-x_2)-\delta}{(0.01+x_2)+\delta}\right|. \tag{7}$$

To make the above computation sufficiently precise, we change the interval of integration, taking $x_1 = 0.1$, $x_2 = x_f - 0.1$, thus, making the interval of zone B smaller improves the precision of the value T_r. Similar to the above method, the time of establishment of a pulse obtained by computation is

$$T_r - T'_1 - t_1 = \frac{1}{a}\ln\left(1+\frac{n_1-n_2}{20\varphi_1}\right) + \frac{1}{b}\ln\left|\frac{(0.1-x_2)-\delta}{(0.1-x_2)+\delta}\right|. \tag{8}$$

where T'_1 corresponds to the time interval of the interval (0, 0.1) of integration, t_1 corresponds to the time interval of the interval (x_p, 0.1) of integration.

Similarly, we can define the pulse attenuation time as the time when the density of the number of photons progresses from ψ_p to the end value

$$T_f - t_2 - T'_2 = -\frac{1}{b}\ln\left|\frac{x_f-x_2-0.1-\delta}{x_f-x_2-0.1+\delta}\right| + \frac{1}{C}\ln\left[1+\frac{n_2-n_f}{20\varphi_2}\right]. \tag{9}$$

where T'_2 corresponds to the time interval of the interval (x_f, x_f -0.1) of integration, t_2 corresponds to the time interval of the interval (x_p, x_f -0.1) of integration. The factor $C = 1 - \frac{n_f}{n_p}$.

The results listed in Table 1 show that when $n_1 / n_p \leqslant 11$, the errors between the values of T_r calculated from equation (8) and the computer results are smaller than 5%.

Table 1. Comparison of the values of T_r and computer results

(1) n_1/n_p	1.221	1.492	2.014	3.004	4.956	6.050	9.026	11.023
(2) T_r 计算值	99.4	47.8	24.6	13.1	6.96	5.54	3.59	2.92
(3) T_r 计算机值	98.1	47.5	24.5	12.8	6.71	5.32	3.43	2.78

(4) 注: T_r 值均以 T 为单位.

Key: 1. n_1 / n_p
2. Computer solution of T_r
3. Value of T_r calculated from equation (8)
4. Note: The values of T_r are all in units of T.

II. Single Pulse Condition and Analysis

1. Establishing the Single Pulse Condition

According to reference (2) and equation (8) in the previous section, we can determine the single pulse condition as

$$\frac{1}{a}\ln\left(1+\frac{n_i-n_p}{20n_i}\right)+\frac{1}{b}\ln\left|\frac{(0.1-\varepsilon_2)-b}{(0.1-\varepsilon_2)+b}\right| > t'_s \qquad (10)$$

Here, the switching time t'_s is in units of T.

The above equation shows that to obtain single pulse output, we must adjust the time of establishment T_r of the pulse or the switching time t_s, it is best to adjust these two times to be nearly equal. Because of the relationship of the logarithmic function, obviously, the magnitude of T_r is mainly determined by the factors a and T, i.e., determined by the inverse density n_i of the initial number of particles, the inverse density n_p of the number of particles of the threshold value, the length of the cavity L and the loss coefficient r. But to obtain the largest energy output, we must seek the best penetration coupling (6), therefore the magnitude of T_r is mainly determined by n_i, n_p and L. The larger the n_i, the lower the n_p, or the shorter the L, the faster the T_r. Because n_i and n_p are both miscroscopic quantities, from equation (1) in reference (2) we know n_i is determined by the pumping power. Therefore, as the pumping power increases, the value of T_r reduces, thus multiple pulses are easily produced.

In addition, according to the threshold conditions, n_p is directly proportional to $2\pi\tau\Delta\nu$, while the value of $2\pi\tau\Delta\nu$ increases as temperature increases, therefore T_r increases as temperature rises. If a device can generate a single pulse under room temperature, then under low temperatures, it can easily produce multiple pulses of low power. This is consistent with the experimental results (8). Also, because the threshold value n_p is directly proportional to the active section S, therefore as the active section increases, T_r becomes larger, and a single pulse is more easily obtained.

2. Obtaining Single Peak and Multiple Peak Zones

If we use the inverse density n_i of the initial number of particles as the vertical coordinate and the switching time t_s as the horizontal coordinate as in Figure 1, then according to equation (10) and the threshold value condition, we can obtain the three zones, I, II and III. The boundary of zone I and zone II is the stationary threshold value, and the boundary of zone II and zone III is the curve of the equality in equation (10). Thus, in zone I, because the initial inverse density of the number of particles is too low, no pulse is output, while zone II is the single pulse output zone, zone III is the multiple pulse output zone.

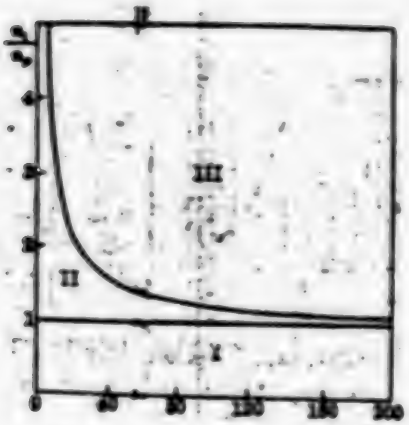

Figure 1. Single Peak and Multiple Peak Operating Zones

In addition, the length of the cavity L can be used as the vertical coordinate and the $1/t_g'$ can be used as the horizontal coordinate to draw the single peak and multiple peak zones under different pumping levels ($1/t_g'$ is measured in units of $C \cdot r \times 10^{-3}$). The upper right of each curve is the single peak zone and the lower left is the multiple peak zone, as shown in Figure 2.

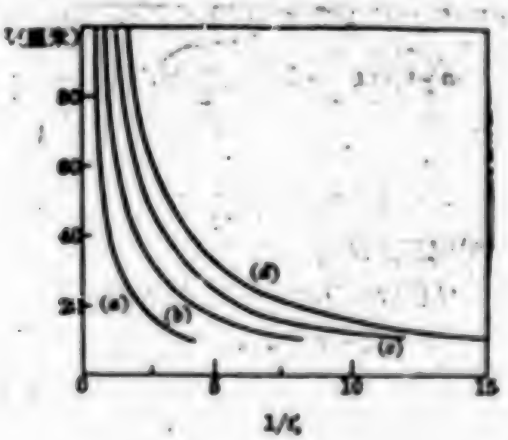

L (centimeter)

Figure 2. Single peak and multiple peak output zones using cavity length L as the variable under different pumping levels

a—n_i/n_p=3.014; b—n_i/n_p=3.004;
d—n_i/n_p=4.065; d—n_i/n_p=4.953

It can be seen from Figure 2 that if the switching time t_g' is given, then to obtain a single peak output, the shorter the cavity length, the smaller the maximum value of n_i / n_p allowable. The longer the cavity, the higher the maximum value of n_i / n_p allowable. This coincides with experimental results[5].

III. Analytic Description of the Oscillation Process

To find the characteristics of variation of the inverse density n of the number of particles and the density ψ of the number of photons along with time, we must

first find the relationship of n and ψ with the variable x. We can derive the relationship of n and ψ with the variable x from assumption (3) in the previous section and equation (11) in reference (1) as

$$n = n_0 e^{-\sigma x} \tag{11}$$

and

$$\varphi = \frac{n_2}{2} \dot{x} \tag{12}$$

then we can find n(t') and ψ (t') from the relationship between t' and x, x is directly proportional to the area encircled below the curve of the expansion of the density ψ (t) of the number of photons along the time axis, i.e., x represents the energy parameter of the laser.

In the following, we first find the n and ψ of the A zone ($0 \leqslant x \leqslant 0.1$) as

$$n = n_0 \exp\left[-\frac{2\sigma_0}{n_2 c}\left(\sinh \frac{at'}{2}\right)\left(\exp \frac{1}{2} at'\right)\right] \tag{13}$$

$$\varphi = \varphi_0 e^{at'}. \tag{14}$$

taking t = 0 as the origin of time.

The n and ψ in the B zone ($0.1 \leqslant x \leqslant x_f - 0.1$) are

$$n = n_0 \exp\left[-b \tanh \frac{1}{2} b(t' - t_p) - \varepsilon_p\right] \tag{15}$$

$$\varphi = \varphi_p \operatorname{sech}^2 \frac{1}{2} b(t' - t_p) \tag{16}$$

the origin of time is at t_p.

The n and ψ in the C zone ($x_f - 0.1 \leqslant x \leqslant x_f$) are

$$n = n_0 \exp\{-\varepsilon_f + 0.1 \exp[-C(t' - T_2)]\} \tag{17}$$

$$\varphi = \frac{n_2 \cdot C}{20} \exp[-C(t' - T_2)] \tag{18}$$

The origin of time is the time t_2 corresponding to x_2.

The above equations show that the inverse density n of the number of particles in zone A drops exponentially, the density ψ of the number of photons increases exponentially with time, therefore, zone A is a rising zone or a growing zone. Zone B is the zone where the main peak of the pulse is, n attenuates drastically, when point t_p reaches n_p, the time distribution of the main peak of the light pulse is a square type hyperbolic secant function, not a Gaussian type. At point

t_p the peak value ψ_p is reached. In zone C, n and ψ both exponentially attenuate to the final values. Figure 3 shows a diagrammatic description of the variation process of n and ψ .

Equation (16) shows that the shape of the part of the main peak of the pulse is symmetric, and from that equation, we can calculate the half maximum full width (HMFW) of the pulse

$$\delta' = \frac{3.53}{b} \tag{19}$$

or

$$\delta = \frac{3.53}{b} T \tag{20}$$

Equation (20) shows δ is determined by b and T, and it is also determined by n_i, n_p, L and r, and the method of analysis is the same as in the previous section, and we can conclude that the higher the pumping power or the shorter the cavity or the lower the temperature, the narrower the pulse width, and vice versa. The effects of the pumping power and the length of the cavity upon the output pulse width coincide with the experimental results[5]. Similarly, the effects of the active section S upon the pulse width can be predicted. The larger the S the wider the pulse width. Figure 4 shows the corresponding narrowing of the pulse width as the value of n_i / n_p increases.

Figure 5 shows a comparison of the two kinds of computational results of the pulse wave form. In the central region, the two coincide very well and they differ only slightly at the lower part of the two wings of the curves.

Table 2 lists the comparison of the two kinds of computational results of the pulse width. For values of δ' , the error between these values and the computer solutions when n_i / $n_p \leqslant 6$ is less than 10%, when n_i / $n_p \geqslant 6$ and n_i / $n_p \leqslant 11$, the error is within 20%, and the two basically coincide.

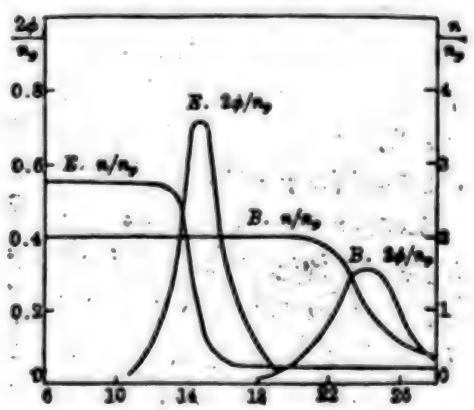

Figure 3. Pulse Oscillation Process

t' is measured in units of T.

$$B\frac{n_i}{n_p} = 2.014;\ \frac{2p_2}{n_p} = 0.314$$
$$E\frac{n_i}{n_p} = 2.718;\ \frac{2p_2}{n_p} = 0.718$$

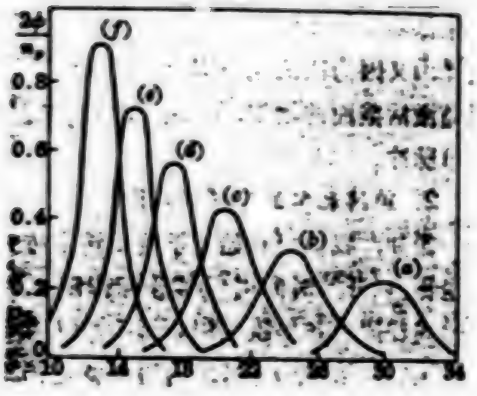

Figure 4. Variation in Pulse Width

a—n_1/n_0=1.822; b—n_1/n_0=2.016; c—n_1/n_0=2.220; d—n_1/n_0=2.460; e—n_1/n_0=2.718; f—n_1/n_0=3.004

t' is in units of T.

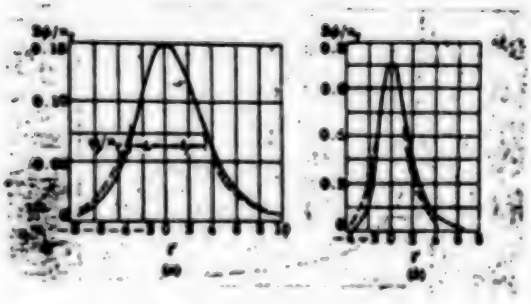

Figure 5. Comparison of the Analytic Solution and the Computer Solution of the Oscillating Waveform of the Light Pulse

(a)—n_1/n_0=1.649; (b)—n_1/n_0=2.718

Solid line is the computer result; dotted line is the analytic result, t' is time in units of T.

Table 2. Comparison of the Results of the Two Methods of Computation of the Pulse Width

	n_1/n_2	1.221	1.492	2.014	3.004	4.958	6.050	9.025	11.023
(1)	δ' 计算机解	16.4	8.25	4.50	2.70	1.75	1.53	1.23	1.13
(2)	δ' 按(20)式计算	17.1	8.24	4.46	2.63	1.68	1.88	1.04	0.91

Key:
1. δ' Computer solution
2. δ' Calculated according to equation (20)

References

(1) Wagner W. G., Lengyel, B.A. JAP, 1963, 34, 2040.

(2) Vuylsteke A.A., JAP, 1963, 34, 1615.

(3) Writing Group of Laser Physics; "Laser Physics", 1975, 215.

(4) Dr. Dieter Ross, Laser Light Amplifiers and Oscillators, 1969, 340.

(5) Arecchi F. F. et al, "Nuovo Cimento," 1964, 34, 1458.

(6) Huang Hongjia [7806 1347 0857]; "Chinese Science", 1974, 3, 247.

(7) Song Mingzhao [1345 6900 6856]; "Laser", 1978, 5, No 5-6, 28.

(8) Benson R.C., Mirarchi M. R.; IEEE Trans., 1964, Mil-8, 13.

9296
CSO: 4008/421

STRUCTURE, OUTPUT CHARACTERISTICS OF PULSED XENON ION LASER

Shanghai JIGUANG [LASER JOURNAL] in Chinese Vol 8 No 4, Apr 81 pp 18-21

[Article by Wang Yuzhi [3769 3768 5347], Xie Peiliang [6200 1014 5328], Dong Jingxing [5516 2529 2502], and Feng Bingfang [7458 3521 5364] of the Shanghai Optics and Fine Mechanics Institute of the Chinese Academy of Sciences: "The Pulsed Xenon Ion Laser." This article was received on 20 February 1980]

[Text] Abstract This article reports on a small pulsed Xe ion laser. The peak power of the laser is 150 watts, 10 oscillating spectral lines are found in the 4300 to 6300 angstrom range, the pulse width of the laser is 0.2 to 1 microsecond, the discharge voltage is 4 to 12 kilovolts, the gas pressure is 0.1 to 9 millitorr.

Structure of the Device

The experimental device is shown in Figure 1.

The laser is 1600 millimeters long, discharge length is 1100 millimeters, the diameter is 3.8 millimeters, the gas chamber is 1000 millimeters long, the diameter is 15 millimeters.

Because the pressure of Xe gas is unstable, it will affect the stability of the output power. Instability of pressure is caused by two reasons. One is the gaseous pump effect which forms a gas pressure difference at the two ends of the laser tube. This difference in gas pressure can be approximated as[1]

$$\Delta P = 6.7 \times 10^{-10} PITfL(D)^{-3}$$

where P is the pressure of the gas in the tube, I is the peak electric current, T is the electric current pulse width, f is the repetition frequency, L, D are respectively the length and diameter of the laser tube. We know that appropriately shortening the tube and increasing the diameter of the tube are good for stable discharge. The second is the absorption of Xe gas by overheating and gasification of the quartz tube and the cathode. We have used the gas storage device to stabilize the pressure of the Xe gas.

This type of laser needs a higher discharge electron density[2], the typical numerical value surpasses 10^{13} /centimeter^3. First we used a molybdenum tube cathode of ϕ 20 x 20 millimeters, although laser output was obtained, but the

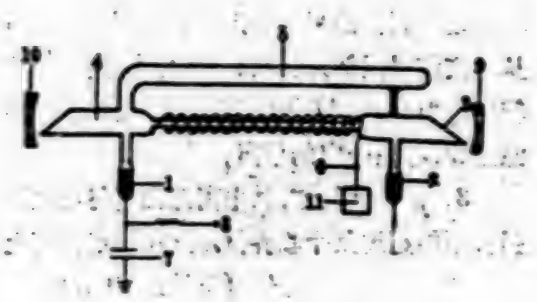

Figure 1. Pulsed Xe ion laser

Key:

1. Cathode
2. Anode
3. Brewster window
4. Laser
5. Gas storage
6. Trigger filament
7. Capacitor
8. Resistor
9. Cavity mirror with a penetration of 12%
10. Aluminum plated fully reflective mirror
11. Trigger power source

discharge voltage was high. Therefore, we used a cold cathode of pure metallic indium[3]. The electric current density which this type of electrode bears surpasses 2000 ampere/centimeter^2. Metallic indium that was 99.999% pure was melted in air and then sealed around the tungsten rode electrode and we carefully avoided air bubbles from entering the indium. During the course of melting indium, the oxide surface formed was not specially treated.

The demand for purity of the gas is also high. Therefore, the system requires a vacuum as high as 10^{-6} torr, and during the course of filling gas, a molecular sieve is used to effectively adsorb vapor and other impure gases. At the same time, discharge treatment of He gas and Xe gas in the discharge tube is also carried out.

The radius of curvature of the cavity mirror is 4000 millimeters, the phase distance is 1700 millimeters. At one end is an aluminum plated fully reflecting mirror. The other end is plated with a multi-layered media film, the penetration is 12%.

The voltage of the power supply is 4 to 12 kilovolts, the discharge capacitance is 0.28 microfaraday, the laser pulse width is 0.2 to 1 microsecond, the peak pulse power is 150 watts.

At present, this laser can continue to operate over 10^4 times after one filling of gas and no visible energy attenuation is observed.

Output Characteristics

1. Laser Spectral Line

The Xe ion laser's energy level structure determines that there will be many oscillating spectral lines. The arrangement of the basic state electrons of the Xe atom is $5P^6$, when undergoing electron collision, the following two types of jumps occur:

$$5P^6 + e \longrightarrow 5P^5\,ms + e$$

$$5P^6 + e \longrightarrow 5P^5\,md + e$$

Here, m = n + 1, n + 2, n + 3,...., n = 5.

We used the WDS-1 model monochromatograph and measured the oscillating spectral lines in the visible light range. Because the central wavelength and the reflection of the reflecting mirror are not the same, 10 different laser oscillating spectral lines were found, for details see Table 1.

It can be seen from Table 1 that when the central wavelength of the reflecting mirror varies from 4300 angstroms to 6300 angstroms, the spectral lines that oscillate most easily are the 5956 angstroms (orange red), 5260 angstroms and 5359 angstroms (two green lines) lines.

Table 1. Relationship between the central wavelength of the reflecting mirror and the oscillating spectral lines

Central wavelength of the reflecting mirror (Å)	Oscillating spectral line (Å)
4300	5359, 5260, 5044, 4954, 4306
5300	5956, 5359, 5353, 5260, 5190, 5044, 4954
5900	5956, 5359, 5260
6300	6270, 5956, 5600, 5359, 4954

Especially worth pointing out is that when the central wavelength of the reflecting mirror is 5900 angstroms, under a gas pressure of 3 to 9 millitorr, within the voltage of 6 to 10 kilovolts, there is only one orange red line of 5956 angstroms. But, when the reflection of the cavity mirror is very low, oscillation is also produced[4]. Utilizing this characteristic in the laboratory, it can be suitably used as the light source of monochromatic pulse.

When the central wavelength of the reflecting mirror is 6300 angstroms, we fix the voltage at 9 kilovolts and change the gas pressure. We can see that when the gas pressure is 8 millitorr, the three spectral lines of 6270 angstroms, 5956 angstroms, 5600 angstroms occur. When the gas pressure drops to 6 millitorr, besides the three spectral lines mentioned above, a jump to the 5359 angstroms line which is shorter than the 5600 angstroms line occurs. When the gas pressure continues to drop to 3 millitorr, the long wavelength of 6270 angstroms disappears, and an oscillating 4954 angstroms line which is even shorter than 5359 angstroms appears.

When the gas pressure is fixed at 6 millitorr, changing the voltage will also cause a change in the oscillating wavelengths. When the voltage is 7 kilovolts, the four spectral lines of 5956 angstroms, 5600 angstroms, 5359 angstroms, 5260 angstroms appear. When the voltage rises to 9 kilovolts, oscillation moves towards the short wavelengths, and the 4600 angstroms line (purple light) appears.

It can be seen from the above experiment that the jumping wavelength changes with voltage and gas pressure[2]. The lower the gas pressure, the higher the voltage, the more easily short wavelength oscillations occur.

2. Pulse Energy

In the experiment, we used the calibrated calorimeter and measured the output energy of the single pulse to be 0.6 millijoules/pulse. At the same time, we measured the effect of the discharge voltage and the filling gas pressure upon the output energy.

a. The relationship between the discharge voltage and the pulse energy is shown in Figure 2.

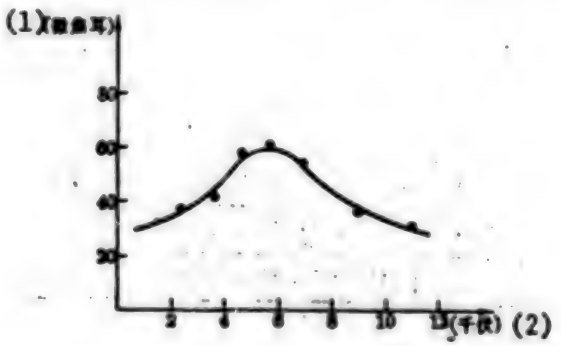

Figure 2. Relationship between discharge voltage and pulse energy

Key:
1. Microjoules
2. Kilovolts

It can be seen from Figure 2 that when the discharge voltage surpasses the threshold value, the pulse energy increases as the voltage increases, when the energy increases to a certain maximum value, as the voltage rises, the energy gradually drops. In the experiment, we kept the gas pressure unchanged at 2 millitorr, therefore as the discharge voltage increased, the value of E/P increased. The best E/P value we obtained was 2.5×10^4 volt/centimeter·torr. Continued increase in the discharge voltage caused the laser to deviate from the best E/P value, therefore the pulse energy dropped.

b. The relationship between the operating gas pressure and the pulse energy is shown in Figure 3.

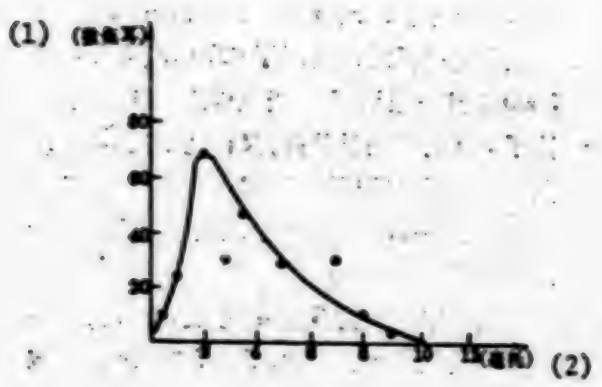

Figure 3. Relationship between operating gas pressure and pulse energy

Key:

1. Microjoules
2. Microtorr

It can be seen from Figure 3 that when the voltage is fixed, after the gas pressure in the tube surpasses the threshold value, the pulse energy increases rather quickly as the gas pressure increases. When the energy increases to a certain maximum value, continued increase in gas pressure will cause the laser output to drop relatively quickly.

When the voltage is fixed and as long as the average electron energy is sufficiently high, after the gas pressure surpasses a threshold value, as the gas pressure increases, the number of particles in the excited state produced by ionization becomes larger, therefore the output of the laser also becomes larger. But the result of an overly high gas pressure is that the chance of collision of particles increases, the free range reduces, the average electron temperature drops, therefore the pulse energy drops.

3. Laser Pulse

a. Changes in pulse width with gas pressure

The oscillographic photos of the changes in pulse width with gas pressure are shown in Figure 4.

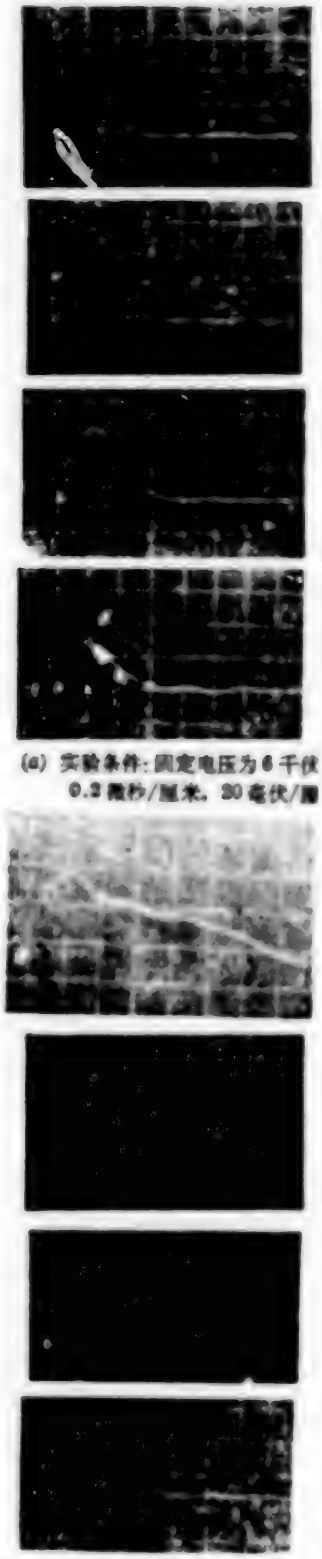

Key:

1. 4 millitorr
2. 3.5 millitorr
3. 2 millitorr
4. 1.2 millitorr
5. (a) Experimental condition: fixed voltage of 6 kilovolts, oscilloscope 0.2 microsecond/ centimeter, 20 millivolt/ centimeter
6. 5.5 millitorr
7. 4 millitorr
8. 3 millitorr
9. 1.8 millitorr
10. (b) Experimental condition: fixed voltage of 10 kilovolt, oscilloscope 0.2 microsecond/ centimeter, 20 millivolts/ centimeter

Figure 4. Oscillographic photos of the relationship between gas pressure and pulse width

The curve showing the relationship between the pulse width and the gas pressure is shown in Figure 5.

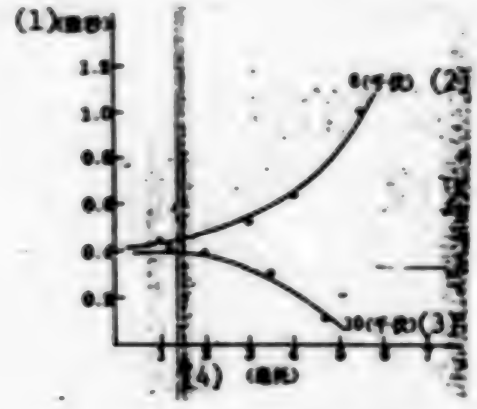

Figure 5. Relationship between pulse width and gas pressure

Key:

1. Microsecond
2. 6 (kilovolt)
3. 10 (kilovolt)
4. Millitorr

It can be seen from Figure 5 that when the discharge voltage is slightly higher than the threshold voltage (about 6 kilovolts), as the gas pressure rises, the pulse width increases, and when the voltage increases to 10 kilovolts, the exact reverse change occurs, i.e., as the gas pressure rises, the pulse width becomes narrow.

b. The relationship between the pulse width and the excitation voltage is shown in Figure 6.

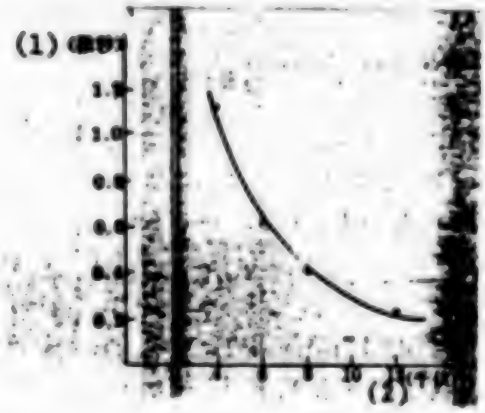

Figure 6. Relationship between pulse width and excitation voltage

Key:

1. Microsecond
2. 12 (kilovolts)

It can be seen from Figure 6 that the laser pulse width becomes narrow as the discharge voltage rises[5].

The above is a description of the characteristics of the pulsed Xe ion laser. One of the uses of this type of laser is to serve as the pump source of the dye laser. Because the pumping line of the ion laser is close to the maximum absorption line of the dye laser, therefore the pumping efficiency is higher.

In addition, in the laboratory, we can regard the pulsed Xe ion laser as a coherent light source to study the discharge evenness in the temperature field, the flow field and plasma.

Figure 7 shows the interference in the temperature field of a flame photographed by the Mach-Zehnder interferometer using the Xe ion laser.

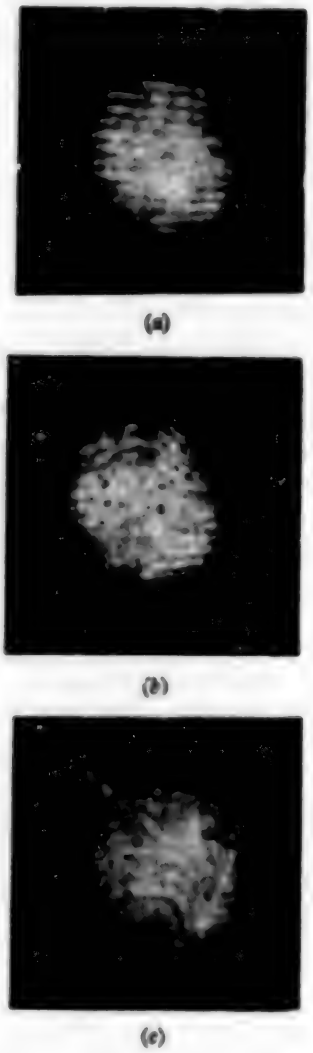

Figure 7.

(a) Photograph showing interference when there is no flame; (b), (c) Changes in the lines of interference caused by temperature distribution when a flame is placed in the light path.

References

(1) Clinton D.H., Rev. Sci. Instrum., 1974, 45, 400.

(2) Bridges W.B., Appl. Phys. Lett., 1964, 4, 178.

(3) Simmons W.W., IEEE J. Q. E., 1970, QE-6, 649.

(4) Willian W.S., IEEE J. Q. E., 1970, QE-6, 466.

(5) Bridges W.B., Appl. Opt., 1965, 4, 573.

9296
CSO: 4008/421

CHARACTERISTICS OF PULSED GOLD VAPOR LASER OUTLINED

Shanghai JIGUANG [LASER JOURNAL] in Chinese Vol 8 No 4, Apr 81 pp 45-46

[Article by Zhang Guiyan [1728 2710 3601], Liang Baogeng [2733 1405 2704], Jing Chunyang [2529 2504 7122], Yin Xianhua [1438 2009 5478], Ye Yanjie [5509 1693 3381], Cang Yongqing [0221 3057 3237] of the Shanghai Optics and Fine Mechanics Institute of the Chinese Academy of Sciences: "Pulsed Gold Vapor Laser." This article was received on 25 July 1980]

[Text] At present, metallic vapor lasers are an active field. Several dozen laser oscillating spectral lines have been found within the very broad spectral wavelengths from infrared to ultraviolet. We have carried out laser studies of gold vapor on the basis of copper vapor laser studies and obtained a pulsed laser of gold atoms of an operating wavelength of 6278 angstroms.

I. Experimental Setup

The characteristic of the gold vapor laser is that it can operate in high temperatures and highly repetitive frequency pulses. The experimental setup includes a gas discharge tube of special structure, a highly repetitive frequency pulse excitation power source, an optical harmonic oscillation cavity and a checking system, as illustrated in Figure 1. The special gas discharge tube is made of a quartz tube of ϕ_{inner} 12 x 300 millimeters, the inner lining is a transparent oxidized aluminum porcelain tube of ϕ_{inner} 8 x 260 millimeters. The outer casing is a fused quartz thermal insulation case of ϕ_{outer} 30 millimeters. In the sandwiched layer is a thin multilayer molybdenum plate serving as an insulating layer. Inside the thermal insulation case is a vacuum. The two ends of the discharge tube are optical quartz windows. The plane of the windows is slanted at a 3° inclination away from the perpendicular direction of the light axis. On the two ends of the discharge tube are pure tungsten rod electrodes of ϕ 6 x 50 millimeters vacuum cealed onto the tube by molybdenum plates, the distance between the electrodes is 290 millimeters. The structure of the discharge tube is shown in Figure 2. The vacuum in the tube is 2×10^{-4} torr, neon buffer gas of 26.5 torr fills the tube and spectrographically pure gold powder of 5 grams are placed in the tube. It needs to be especially pointed out that the buffer gas induces discharge and propagation of energy, it can also slow the diffusion of the metallic vapor towards the two ends of the discharge tube and serves definitely to protect

the optical windows. The optical harmonic oscillation cavity consists of a totally reflective film with a curvature radius of 3 meters and an optical plate with a penetration of 19%. The length of the cavity is 755 millimeters. The multiple repetitive frequency pulse excitation power source is a Blumlein harmonic charge circuit triggered alternately by the pulse thyratron. The high temperature of the discharge tube is sustained by self heading during discharge, temperature measurement is done by the use of a platinum-platinum rhodium thermal coupler in the thermal insulation layer combined with the 902 model automatic temperature controler.

Under our experimental conditions, the power supply voltage was 3750 volts, the charge inductance was 0.4 henry, the capacitance was 2 microfaraday, the repetitive frequency of the pulse was 16 kilocycles, the light emission occurred 30 minutes after discharge, maximum output occurred about 10 minutes afterwards, and the device operated in a stable manner.

II. Experimental Results

In the experimental device described above, we obtained a 6278-angstrom pulsed laser with an average output power of 35 milliwatts, operating in a stable fashion for 7.5 hours. We used a combination of the 1P-21 photoelectric multiplier and a WDS-J2 model circular disc monochromatograph and measured the maximum half width of the laser pulse to be 32 millimicroseconds. We used the WPG-100 model plane grid spectrograph and photographed the emitting spectrum of the gold vapor laser and carried out wavelength calibration using the double line of the sodium spectrum and the He-Ne laser spectral line as control source, see Figure 3.

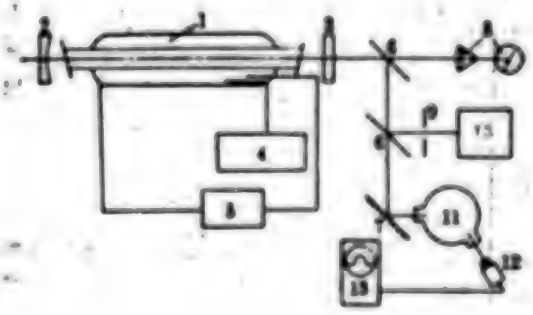

Figure 1. Experimental setup of the pulsed gold vapor laser

Key:

1. Discharge chamber
2. Fully reflective medium film
3. Partially reflective medium film
4. Temperature measurement
5. High frequency pulse excitation power source
6. Spectrometric plate
7. Fully reflective film
8. Power measurement
9. Small aperture stop
10. Spectroscope
11. Monochromatograph
12. Photoelectric multiplier
13. Oscilloscope

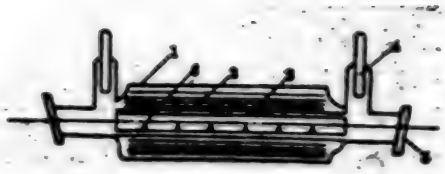

Figure 2. Structure of the discharge tube

Key:

1. Fused quartz outer shell
2. Molybdenum plate thermal insulation layer
3. Porcelain lining tube
4. Tungsten rod electrode
5. Quartz window
6. Pure gold

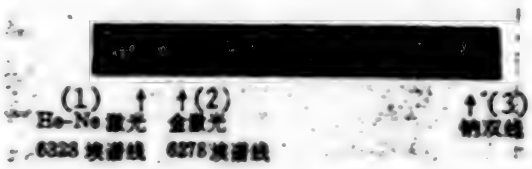

Figure 3. Gold vapor laser emission spectral lines

Key:

1. He-Ne laser
   6328 angstrom spectral line
2. Gold laser
   6278 angstrom spectral line
3. Sodium double line

References

(1) S.V. Markova, G.G. Petrash, Sov. J. Quant. Electr., 1978, 8, No 7, 904-906.

9296
CSO: 4008/422

LASER TRIGGERED SPARK GAPS UNDER EXPERIMENTAL STUDY

Shanghai JIGUANG [LASER JOURNAL] in Chinese Vol 8 No 4, Apr 81 pp 46-47

[Article by Meng Shaoxian [1322 4801 6343], Pu Chaoshun [3184 2600 7311], Yang Yi [2799 5030], Sun Naigeng [1327 0035 1649], Xie Ziming [6200 2737 6900] of the Shanghai Optics and Fine Mechanics Institute of the Chinese Academy of Sciences: "Experimental Study of Laser Triggered Spark Gaps." This article was received on 21 December 1979]

[Text] Laser triggered spark gaps[(1)] are an important component for the selection of singular ultrashort pulses from the locked mode pulsed laser and for shearing of laser waveforms by the photoelectric switch.

We first experimented with the copper sphere gap. It consists of two copper spheres of ϕ 20 millimeters. The multiple voltage rectified high voltage is passed through a 75 ohm electrical cable which is connected to the spheres. When the locked mode laser passes through the short focal distance lens and focuses on the gap between the copper spheres, an air puncture is formed producing initial electrons and ions. These electrons and ions move towards the two electrodes under the effects of the electrical field of the gap between the spheres, thus forming a puncture in the gap between the spheres.

To measure the discharg waveform in the gap between the spheres, we used the T type four terminal network attenuator connected to an OK-19 high voltage oscilloscope for photographing, the sensitivity of the oscilloscope was 280 volts/centimeter, the rising time was 2.25 millimicroseconds, the clock marked a gap of 10 millimicroseconds between peaks of the wave.

The fore of the waveform of the switch discharge in the gap between copper spheres is longer, when a 20,000-volt voltage is added to the gap between the spheres, the distance of the gap between the spheres is 6 millimeters, but when the humidity of air is large, the distance should be appropriately lengthened. We used a formed electrical cable of 1 meter long. The photographed waveform in the gap between the spheres is shown in Figure 1. Using the 75 ohm electrical cable, the rising time in the gap between the spheres is 7 millimicroseconds. The gap between copper spheres is generally not too stable, when the humidity of air changes, the puncturing voltage will change.

Figure 1. Discharge waveform in the gap between copper spheres (distance between peaks of the wave is 10 millimicroseconds)

To obtain a spark gap with a faster rising time requires a reduction of the distance between the two electrodes of the spark gap. This means that a medium of good insulating properties must be added between the two electrodes of the spark gap.

According to Paschen's empirical curve, we conducted a spark gap experiment using xenon filled low pressure glass, the filling gas pressure was 10^{-3} to 10^{-4} torr.

We discovered in the experiment that, for this type of spark gap, when the voltage is relatively high, puncturing does not occur at the closest distance to the electrode but long distance discharge is formed and a so-called "long range effect"[2] occurs, affecting the rising time of the spark gap. In addition, this type of spark gap is unstable, after several discharges, because the electrodes release gas, the puncture voltage is changed.

For this, we conducted a spark gap experiment using high gas pressure silicon dioxide glass. For high gas pressure, we used liquid nitrogen to make cold krypton gas and injected it into the silicon dioxide tube and then changed it back to a gas. The distance between the electrodes of this type of spark gap can be very close, the experimental curve is shown in Figure 2. It can be seen from the diagram that when the distance between the electrode is fixed, the increase in gas pressure will cause a corresponding increase in puncture voltage.

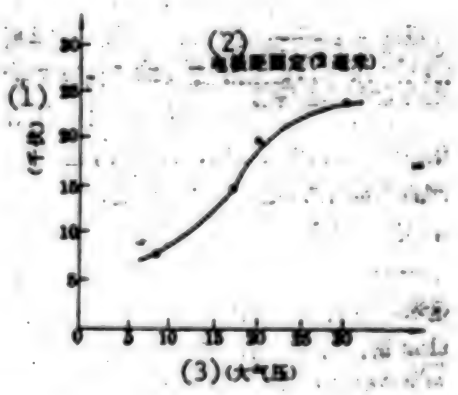

Figure 2. Relationship between puncture voltage and gas pressure

Key:

1. Kilovolt
2. Fixed distance between electrode (2 millimeters)
3. Atmospheric pressure

This type of spark gap also has a definite shortcoming. When using a short focal distance lens to focus the laser to puncture the spark gap, the quartz tube wall cannot bear the radiation of the laser, and also, the gas pressure cannot be easily controlled, and the distance between the electrodes cannot be adjusted.

Later we used a spark gap with a metallic chamber of high gas pressure with an adjustable distance between the electrodes and an adjustable gas pressure. This kind of a device uses stainless steel as electrodes, its escape power is larger, and at the same time, it does not easily react with the filling gas. We selected nitrogen gas, the gas pressure was 20 atmospheric units, for laser focusing, we used the 1:5 lens, the focal distance was 10 centimeters. When the spark gap and the Pockels cell switch are connected, the discharge waveform produced by using a locked mode laser to puncture the spark gap is shown in Figure 3.

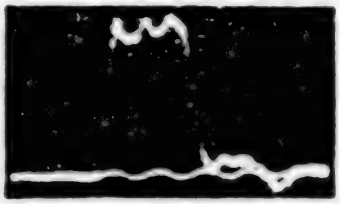

Figure 3. Discharge waveform of a high voltage spark gap

At this time, the capacity of the KDP crystal of the Pockels cell is 5 micromicrofaraday, the characteristic impedance of the electrical cable is 75 ohms, the distance between the electrodes is 0.8 millimeter, the voltage is 23,000 volts, the rising time measured is 1.6 millimicrosecond. If a low electrical resistance cable is used, the rising time will be even faster. In Figure 3, the fluctuation of the voltage is mainly caused by the incomplete matching of the dynamic resistance and impedance of the spark gap.

In addition, we also conducted an experiment of the gap between spheres using a solid medium--polytetrafluoroethylene plastic as the insulating material. This type of medium can have a higher tolerance to voltage but it easily allows electrical creeping about the medium, the puncture voltage is affected by the cleanliness of the medium, and after each puncture, branch like patterns appear on the medium and it cannot be used further.

We also conducted experiments of the gap between spheres using transformer oil as the insulating material. Its insulation is not too good, during each puncture, gas bubbles emerge from the oil, and the insulation of the medium also changes gradually. The principles for each gap between spheres we used are illustrated in Figures 4 and 5.

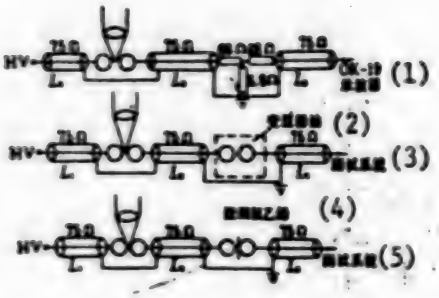

Figure 4. Several types of pulse forming circuits in the gap between copper spheres

Key:

1. Oscilloscope
2. Transformer oil
3. Testing system
4. Polytetrafluoroethylene
5. Testing system

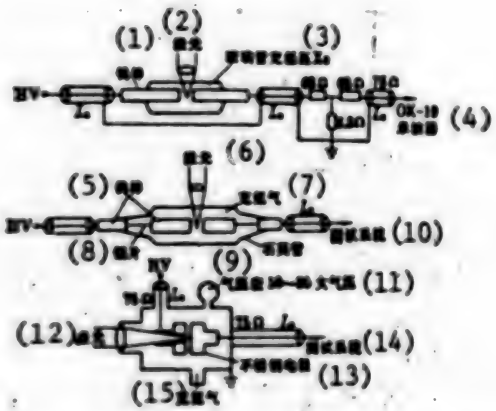

Figure 5. Various types of gas filled gaps between spheres

Key:

1. Tungsten rod
2. Laser
3. Glass tube filled with low pressure Xe
4. Oscilloscope
5. Tungsten rod
6. Laser
7. Filled with krypton gas
8. Molybdenum plate
9. Quartz tube
10. Testing system
11. Gass pressure gauge 10-30 atmospheric pressure
12. Laser
13. Stainless steel electrode
14. Testing system
15. Filled with nitrogen gas

References

(1) A. H. Guenther, Proc. IEEE, 1971, 59, No 4, 689.
(2) Steinmetz, Rev. Sci. Instrum., 1968, 39, 904.

9296
CSO: 4008/422

APPLIED SCIENCES

OPTIC-ACOUSTIC CO_2 LASER SPECTROMETER USED TO ANALYZE, TEST GASES

Shanghai JIGUANG [LASER JOURNAL] in Chinese Vol 8 No 4, Apr 81 pp 52-53

[Article by Chen Chuanwen [7115 0278 2429], Liu Yaotian [0491 5069 3944], Ming Changjiang [3494 7022 3068], Wang Cai [3769 2088], Wang Wenyun [3769 2429 7301], Xu Jun [1776 0193], Li Zhenxiang [2621 2182 4382], Wang Lianjie [3769 6647 2638] of the Changchun Applied Chemistry Institute of the Chinese Academy of Sciences: "Development of the Optic-Acoustic CO_2 Laser Spectrometer." This article was received on 14 July 1980]

[Text] We developed an Optic-Acoustic CO_2 laser spectrometer and used it to analyze and test certain gases such as ethylene and ammonia and obtained the optic-acoustic spectrogram by automatic scanning within the range of the CO_2 emitting spectral lines. The following introduces its structure and function.

Principle and Structural Characteristics

The infrared optic-acoustic testing principle of gaseous samples has been described in detail in past reports(1). Generally speaking, in a sealed optic-acoustic pool, when a gaseous sample is radiated by a modulated light, the light of this wavelength is absorbed by the sample, the thermal motion of the molecules of the gas increases, this is manifested by a periodic wave motion of the temperature inside the pool at the modulated frequency of the incident light, the pressure inside the pool expands and contracts periodically, and a microphone is used to receive the sound frequency pressure signal, and then a locked magnifier is used to detect useful optic-acoustic signals buried in the noise, thus obtaining the optic-acoustic spectrogram of the sample.

The principle and structure of the device is illustrated in Figure 1. The main structures are:

(1) Light source: An extra-cavity tuned CO_2 laser is used as the light source. The range of rotation of the light grid rotary platform is $\pm 5°$, satisfying the requirements of all branch lines of the 00°1 to 10°0 and 00°1 to 02°0 jumps for the azimuth. The laser has 70 to 79 tunable spectral lines, the distribution of its spectral lines are illustrated in Figure 2 and Figure 3.

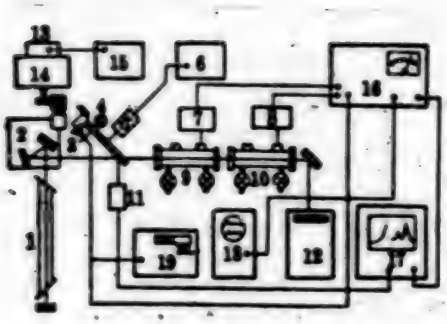

Figure 1. Principle and structure of the optic-acoustic laser spectrometer

Key:

1. CO_2 laser
2. Light grid rotary platform
3. Silicon photoelectric cell
4. Small light bulb
5. Stepwise electric motor
6. Power source of the crystalline stable frequency shearing device
7, 8. Front circuit of the optic-acoustic cell and attenuator
9, 10. Optic-acoustic cell B, A
11. Power meter probe
12. CO_2 laser spectral line analyzer
13. Reversible electric motor
14. Transmission box
15. Scanning circuit controler
16. Locked magnifier
17. x, y function recorder
18. Double line oscilloscope
19. Numerical frequency counter

Figure 2. Optic-acoustic spectrogram of ammonia sample (b) and CO_2 laser power spectrogram (a)

Figure 3. Optic-acoustic spectrogram of ethylene sample (b) and CO_2 laser power spectrogram (a)

(2) Spectral line (wavelength) scanning system: It can be seen from Figure 1 that the scanning system is composed of a long gear and a reversible electric motor attached to the filament rod cap of the light grid rotary platform and fitted to the output gear of the transmission box and a control device. The transmission box can operate in three scanning speeds, 1, 2, and 4 revolutions per minute. The transmission box has a finite switch limiting the light grid to move within an area of rotation of 9 to 11 micrometers, the controler of the reversible electric motor has several shifts of control for positive revolution, reverse revolution, and instant stop and start.

(3) Modulation of the stable frequency of the laser beam: Because the locked magnifier's frequency selection channel requires precision in frequency, when using the synchronous electric motor or the ordinary alternating current electric motor powered by the city's electric power supply for light shearing, the modulated frequency will fluctuate with the city's electrical frequency, if the locked magnifier's frequency selection channel is not adjusted constantly, the output signal will be unstable. For this, we used the quartz crystal stable frequency light shearing device. Its main structure consists of the 96 kilocycle quartz oscillator driving a stepwise electric motor through frequency demultiplication, pulse formation, and power release to lead the light shearing plate for modulation, and a highly stable modulated frequency is obtained.

(4) Monitoring the laser's spectral line: We used the commercial CO_2 laser spectral line analyser to monitor and measure the wavelength of the laser's spectral lines. During the course of scanning, one or two spectral lines are measured on each branch, the others are computed according to the jumping patterns of CO_2.

(5) Detecting and measuring the optic-acoustic cell and the optic-acoustic signals: Introduction to the work in this regard has been described in detail in previous reports(2). The microphone in the optic-acoustic cells A and B must be strictly selected so that the sensitivity, frequency response and base noise must be consistent. Where there is no sample, adjustment of the attenuator can be made so that the optic-acoustic signal of cell A minus cell B equals zero.

Performance of the Device

To prove the correctness of the optic-acoustic spectrogram of the sample measured by the instrument, we selected ethylene and ammonia as the calibrated operating material. Figure 3 shows the optic-acoustic spectrogram of ethylene and the CO_2 laser power spectrogram. Ethylene has a stronger absorption peak at P(14) in the 00° 1 to 10° 0 jump, and a second stronger absorption peak at R(24). (In the diagram, the power spectrum's P(14) peak and the P(14) peak of the sample are at a distance and cannot completely overlap because the x, y recorder's y_1 and y_2 strokes are at a distance apart).

Figure 2 is the optic-acoustic spectrograph of the ammonia sample and the CO_2 laser power spectrogram. Ammonia has relatively strong absorption peaks at P(34), P(32), R(6), R(8), R(14) in the 00° 1 to 10° 0 jump and at P(20), P(34), R(16), R(30) in the 00° 1 to 02° 0 jump. The above spectrograms are all consistent with the reports in reference (1), to examine the quantitative test performance level of the device, we used ethylene as an example to carry out an experiment, when the sample amount was of a low concentration i.e. 0.05 to 1 ppm, repeatable data were obtained. When the sample amount was of high concentration, i.e., 10 to 100 ppm, repetitively stable data were obtained in ten repetitions. A large amount of experimental results show that the sensitivity of this device, i.e., the smallest detectable concentration of ethylene is 0.05 ppm (10^{-8}). When the concentration of the sample is 1 ppm, the greatest deviation of detection is $\pm$20%, the average deviation is $\pm$5%. When the sample amount is 50 ppm, the largest deviation is $\pm$10%, the average deviation is $\pm$20%.

References

(1) R.J. Brewer, C.W. Bruce, Appl. Opt., 1978, 17, 3748.

(2) Chen Chuangwen [7115 0278 2429] et al, LASER, 1980, 7, No 9, 48-51.

9296
CSO: 4008/422

BRIEFS

MICROCOMPUTER FAIR--Beijing, 3 Aug (XINHUA)--A fair to exchange applied technology for microcomputers sponsored by the Hong Kong Jingye Company, the Beijing Economic Construction Company, the Beijing Engineering University and the Institute of Acoustics of China's Academy of Sciences opened in Beijing on 3 August. At the fair, which was scheduled to last 7 days, various microcomputers manufactured abroad were displayed, including the single-board microcomputer model TP-801 jointly designed by the Hong Kong Jingye Company and the Beijing Engineering University. This type of multipurpose microcomputer can be used in teaching, scientific research and industrial and agricultural production. [Beijing XINHUA Domestic Service in Chinese 1532 GMT 3 Aug 81]

CSO: 4008/455

PUBLICATIONS

TABLE OF CONTENTS OF 'DADIANJI JISHU' NO 3, 1981

Harbin DADIANJI JISHU [LARGE ELECTRIC MACHINERY TECHNOLOGY] in Chinese No 3, 1981 preceding p 1

9717
CSO: 4008/412

PUBLICATIONS

TABLE OF CONTENTS OF 'JIGUANG' NO 5, 1981

Shanghai JIGUANG [LASER JOURNAL] in Chinese Vol 8 No 5, May 81 inside back cover

9717
CSO: 4008/418

AUTHOR: CAO Bowei [2580 0130 1983]
et al.

ORG: None

TITLE: "Problems in Housing Development in Shanghai"

SOURCE: Beijing JIANZHU XUEBAO [ARCHITECTURAL JOURNAL] in Chinese No 7, 20 Jul 81 pp 1-5

TEXT OF ENGLISH ABSTRACT: The article puts forward the following three problems in housing development in Shanghai:
1) Building Area and Standards. The authors hold that while increasing the total area of housing to be built each year, efforst should be made to maintain as many suites as possible from the same total building area. To increase the building area of each suite too early will not be favorable in solving housing problems. A better living standard can be obtained as well through other means, such as rational arrangement and more efficient use of space, improvement of interior treatment and multi-purpose furniture.
2) Land and Building Density. The urban area of Shanghai has a population density of 406 persons per hectare. In view of the shortage of usable land and high density of population, residential buildings of 5-6, 8-9 and 12-20 stories in combination should be built. Five to six storied buildings should be emphasized at present, with a gradual increase in height in the coming years. The net building area in the urban district should reach 25,000-30,000 sq m/ha.
3) Standardization and Diversification. Standardization is necessary in housing

[Continuation of JIANZHU XUEBAO No 7, 20 Jul 81]

development. In addition, systematization of typical components should be maintained to meet the demand of diversification of building forms. Diversification does not only concern outward appearance, but also plot plan arrangement, various building types and different combinations of typical units of living room, kitchen, lavatory, etc.

As an analysis of the above points, the authors have prepared alternative schemes for a built-up area for comparison.

AUTHOR: LU Guangqi [0712 0342 4388]
et al.

ORG: None

TITLE: "Planning of Housing Development in Shanghai"

SOURCE: Beijing JIANZHU XUEBAO [ARCHITECTURAL JOURNAL] in Chinese No 7, 20 Jul 81 pp 6-9

TEXT OF ENGLISH ABSTRACT: Eight points on housing development from the viewpoint of city planning are included in the article:
1. In the planning of housing development, which is an important element in the plan of city development, an overall consideration should be given to solve the problems of living, working, studying, communication and recreation. However, housing development is a long-term task which should be adaptable to the changing conditions of the city in economy and culture. Both short-term and long-term considerations should be taken.
2. The distribution of housing development should be in accordance with that of production. The distribution of production in Shanghai is on a dispersed basis. Nine outskirt districts and six satellite towns have been developed since 1949. Four districts, including that north of Pentagon Square, are the main bases for housing development in the near future.
3. To solve the housing problem in Shanghai, organizations and inhabitants in the city center have to be dispersed to satellite towns. However, effects have not been conspicuous due to various reasons. Housing development in satellite towns

[Continuation of JIANZHU XUEBAO No 7, 20 Jul 81]

should be backed by economical, political and communicational supports.
4. The main task of housing development at present centers around extensions and new dwellings on the perimeter of built-up areas. Construction begun in 1980 will house 600,000 people when completed.
5. Rehabilitation of the old city center should be planned overall and properly arranged, adaptive to local conditions and carried out by stages and in groups.
6. Provided that the nature, capacity and distribution of production is well-handled, mixed areas of production and living can be developed. A number of such areas has already been formed in the suburbs.
7. The plan of housing units should be adapted to local conditions, with unit types meeting present requirements of allotment as well as future developments.
8. Housing development should be realized through unified administration and coordinated construction instead of having each organization build its own dwellings. Public buildings and municipal facilities should also be provided in time.

AUTHOR: WANG Dingzeng [3076 1353 3582]
et al.

ORG: None

TITLE: "Design of the Shanghai Hotel"

SOURCE: Beijing JIANZHU XUEBAO [ARCHITECTURAL JOURNAL] in Chinese No 7, 20 Jul 81 pp 16-22

TEXT OF ENGLISH ABSTRACT: The Shanghai Hotel under construction, with 600 twin bed rooms, has a total building area of 44,561 sq m and 26 stories above ground, occupying a lot of 1.02 ha. It is the first large hotel for tourists to be built in Shanghai since liberation.

The architects for the hotel note that the technical means by which problems in design can be solved are just as important as an imaginative artistic conception. Two major purposes are to be fulfilled in hotel design: first, the creation of a comfortable physical environment with adequate facilities, and second, a particular local atmosphere which will give tourists the impression that the trip was worthwhile. Practice in design shows that only when technical problems have been solved can the artistic conception be realized. The whole history of architecture teaches that the development of architectural forms throughout the ages has always been restricted and influenced by technique and materials. Only creative application of technique can turn out a building which is an artistic work of architecture.

[Continuation of JIANZHU XUEBAO No 7, 20 Jul 81]

Nationalistic style or local characteristics is important in hotel design. However, the realization of nationalistic style in highrise buildings is quite difficult. As the interior of a building has more contact with people, the interior design should better satisfy the human demand and expectation. It is also more practical to adopt traditional style in the interior. A strong flavor of Chinese culture can be enjoyed by foreign tourists through interior decoration, furniture and finishing. Silk Road, the ancient passage of communication between the East and West, has been chosen as the leitmotif of decoration in the hotel.

Each type of building has its own particular characteristics. The key points in highrise hotel design are economy, efficiency in space usage and fireproofing. The Shanghai Hotel has an area index of 73.3 sq m/bay, a net area of a twin bed room of 15.9 sq m, and a typical floor height of 3 m, which are on the low side among tourist hotels in China.

AUTHOR: TIAN Wenzhi [3944 2429 0037]
et al.

ORG: None

TITLE: "Shiliupu Passenger Station, Shanghai Port"

SOURCE: Beijing JIANZHU XUEBAO [ARCHITECTURAL JOURNAL] in Chinese No 7, 20 Jul 81 pp 23-29

TEXT OF ENGLISH ABSTRACT: Shiliupu Passenger Station of Shanghai Port is a large one with traffic capacity of 4,350,000 persons per year and 20,000 persons per day. The maximum passenger gathering is 5,832 persons, the area of waiting space 6000 sq m, and the total building area 35,000 sq m.

To separate passenger and goods traffic, Dada Passenger Station in the southern part of Shiliupu, formerly used for inland water traffic, has been turned into a station exclusively for goods, while Shiliupu Station is kept exclusively for passengers.

The station is parallel to the coast line and as near to the berth as possible, leaving more space at the front for approaching. The waiting rooms, ticket office, check room, dispatching office, general office and control room are placed in separate buildings incorporated into a whole with the Passenger Station Building as the major structure. The waiting rooms for different cabins and destinations occupy two floors and include escalators.

[Continuation of JIANZHU XUEBAO No 7, 20 Jul 81]

The building, located at the end of the skyline at the Bund, is the first large public building to be built there after liberation. The architectural treatment, with the dispatching tower and overhead gallery as accents, emphasizes openness and light without affectations.

AUTHOR: FENG Jizhong [7458 4764 1813]

ORG: None

TITLE: "The Garden of the Square Pagoda"

SOURCE: Beijing JIANZHU XUEBAO [ARCHITECTURAL JOURNAL] in Chinese No 7, 20 Jul 81 pp 40-45

TEXT OF ENGLISH ABSTRACT: In the southeastern part of Songjiang, a town within the municipality of Shanghai and about 30 km from the city center, there are three historical relics: a square pagoda of the Song Dynasty which has stood for some 900 years, a nearby screen wall of the Ming Dynasty decorated with brick carvings, and a stone bridge farther away also of the Song. A new garden has been planned to enclose these relics as centers of interest together with the existing old trees and bamboo groves. The garden will have an area of about 11 hectares. In addition to the above-mentioned relics, a temple hall of the Ming Dynasty will be moved from some other location to the garden.

The three relics belong to different ages and bear no relation to one another in space. Any attempt to organize them into a whole by incorporating them with new architectural features would result in failure. Therefore, a free plan has been determined that will keep them as they are, emphasizing the relics themselves as centers of interest. Only terraces, courts, walls, rockeries and ponds are designed to serve as background and means of incorporation. The composition is

[Continuation of JIANZHU XUEBAO No 7, 20 Jul 81]

loose, but not disconnected. The treatment is intended to be refined and simple, recalling the architectural style of the Song.

The ground where the pagoda stands is lower than that of the surrounding area. To eliminate the sunken effect, it is to be enclosed by walls that will form a court, so that the base of the pagoda will not be visible from outside. To give apparent height to the pagoda, the ground outside the court in the eastern approach will wind up and down with steps. No trees or bushes are to be planted in the courtyard, thus giving a sense of solemnity and dominance to the center of interest. Two approaches to the pagoda are designed, a straight one from the north and a winding one among the bamboo groves from the east.

Since the town was called Antler City in ancient times, deer ground is to be provided in the south lawn which slopes down to the water and where maples are to be planted.

The tradition of the Chinese garden still finds its vitality in modern landscape architecture. In order to inherit this tradition, we must comprehend the philosophy, go deep into its ingenuity and absorb its essence. The present day's needs by the large masses could not be met simply by enlarging the dimensions. Foreign experiences in gardening should also be appropriately absorbed. For example, the use of a lawn and the selection of the species of tree as the theme, both to harmonize the whole garden, have been absorbed in its design.

9717
CSO: 4009/439

AUTHOR: None

ORG: Design Department, Fushun Excavator Manufacturing Plant

TITLE: "WD-122 Single Bucket Excavator"

SOURCE: Tianjin GONGCHENG JIXIE [CONSTRUCTION MACHINERY AND EQUIPMENT] in Chinese No 7, 81 pp 1-5

ABSTRACT: The Fushun Excavator Manufacturing Plant most recently succeeded in obtaining the State's certification for its WD-122 excavator. It is, at present, the excavator with a bucket of the largest capacity in China. From Mar 78 to Oct 80, the machine underwent industrial testing at the Anshan Dagushan Iron Mine. Ores weighing 973,000 tons were dug. The machine was in operation continuously for 1821 hours and moved 5.43 km. If transportation vehicles are reasonably coordinated, it can excavate and move 20-30 thousand tons of ore a day, with an average annual productivity of 7,000,000 - 10,000,000 tons. The steel cable averages a useful life of 800,000-1,200,000 tons/piece. Compared with foreign advanced makes, its shortcoming is the thin lubricant used in the speed reducer. Some foreign products now use dry lubricant so that there is no problem of leakage and the cogs of the gears may last longer. At present, the major subject under study in China with respect to excavator manufacturing is the use of silicon controlled power supply.

AUTHOR: XIONG Guoxiang [3574 0948 5046]

ORG: Kunming Municipal Construction Machinery Repair Shop; Kunming College of Engineering

TITLE: "JJKX-1 Fast Winch for Construction Use"

SOURCE: Tianjin GONGCHENG JIXIE [CONSTRUCTION MACHINERY AND EQUIPMENT] in Chinese No 7, 81 pp 5-6

ABSTRACT: The Kunming Municipal Construction Machinery Repair Shop and the Kunming College of Engineering jointly designed and made the JJKX-1 one ton model fast winch for construction use. The prototype underwent 500 hours of industrial testing and fatigue test. In 1980, it was certified. Its major parameters and parts are described, including a photo of the machine. In a table, its parameters are compared with those of similar machines, including the T224-B of the USSR, the KW-10 of Japan, the KUSW-10 of Japan, the TJ-10 of China, the JJK-1 of China, and the JJKX-1 of China.

AUTHOR: DING Bingyun [0002 3521 0061]

ORG: Science and Technology Division, Sichuan Provincial Department of Construction

TITLE: "48-Ton·M Caterpillar Tower Crane"

SOURCE: Tianjin GONGCHENG JIXIE [CONSTRUCTION MACHINERY AND EQUIPMENT] in Chinese No 7, 81 p 7-

ABSTRACT: In order to utilize construction machines to their full capacity, the Mechanized Construction Company No 1 of Sichuan Province reconstructed the 1004 type 15-ton caterpillar crane into the 48-ton·m caterpiller tower crane, adding 25 tons to the maximum lift capacity of the original machine. Due to the high requirement of ground surface condition of this type of crane, and the limitation of the original transmission, which is retained, the speed of rotation is strictly controlled to a maximum of 1 rotation/minute. The device for observing the incline gradient of that machine is in need of further perfecting. The major technical measures used to reconstruct the crane and the parameters of the finished product are described.

AUTHOR: JIN Acheng [6855 7093 1004]
NIU Baozheng [3662 5508 2973]

ORG: Jilin District Highway Construction Machinery Repair and Manufacturing Plant

TITLE: "TP-3500 Towed Asphalt Concrete Spreader"

SOURCE: Tianjin GONGCHENG JIXIE [CONSTRUCTION MACHINERY AND EQUIPMENT] in Chinese No 7, 81 pp 8-9

ABSTRACT: On the basis of all basic capabilities of a self-propelled spreader, i.e. spreading, leveling, weighing down, smoothing, arching, and thickness regulating, etc., the complicated mechanisms for self-propelling, the hydraulic operation, heating the presser, etc. are omitted to produce the TP-3500 towed asphalt and concrete spreader. It is designed to be suitable for ordinary medium and small plants to manufacture, repair, and operate, under the current domestic stage of highway construction. It is simply constructed and inexpensive to make. This paper contains a brief introduction of its structure, including a schematic diagram, and its work principle.

6248
CSO: 4009/444

AUTHOR: LIU Zemin [0491 3419 3046]

ORG: Beijing Institute of Posts and Telecommunications

TITLE: "General Parameter Filter"

SOURCE: Beijing DIANZI XUEBAO [ACTA ELECTRONICA SINICA] in Chinese No 3, 1981 pp 1-10

TEXT OF ENGLISH ABSTRACT: This paper extends the theory of the general parameter filter without the complex loss zeros with quadrantal symmetry. That is, the loss and delay time characteristic of pass-bands is a Chebyshev-type approximation and the loss characteristic of stopbands can be specified arbitrarily. Because the nonminimum-phase transfer function can be expressed as the product of the minimum-phase transfer function and all-pass function, the loss characteristic of non-minimum-phase and corresponding minimum-phase transfer functions is the same and a unique relationship exists between the loss and the phase characteristic of minimum-phase transfer function. A series of new formulas for the loss and delay time function have been derived, and the Chebyshev-type approximation of the delay time characteristic of the pass-band and the initial guess of all available parameters have been obtained. In this respect, this paper presents new ideas and methods. The results of this paper can be used to design varieties of filters, including lumped *LC* filters, active filters, microwave filters, digital filters, etc. The results have been made use of in actual applications and have shown great advantages.

AUTHOR: LIN Yutao [2651 5148 3447]

ORG: Wuhan Digital Engineering Institute

TITLE: "How to Correct Errors of a Position System by Means of a Computer"

SOURCE: Beijing DIANZI XUEBAO [ACTA ELECTRONICA SINICA] in Chinese No 3, 1981 pp 11-18

TEXT OF ENGLISH ABSTRACT: The position system which uses an inductosyn as a transducer can measure the angle and length very accurately. Combining it with the computer constitutes the digital servo system with high precision. This instrument has been broadly used in astronomical navigation, missile controlling, satellite tracking, radar, disk storage, and most kinds of precision machine tools. If the position system works in a static mode, the position error of the transducer will affect the positioning precision. However, once the inductosyn has been made, its position error is fixed, hence we can test its characteristics. In this paper the inductosyn's positional error is analyzed, and from this the mathematical model describing the positional error is formed. The computer can automatically correct the positional error through its error characteristic so that the system's precision of the static positioning will be improved. This is performed by software. "The program for correcting the positional error" written in ALGOL-60 is presented. Because the method is applicable, in principle, to the multipolar rotary transformer, it will be able to make a higher precision position system by use of a lower precision transducer.

[Continuation of DIANZI XUEBAO No 3, 1981 pp 11-18]

When the position system works in the dynamic mode (e.g., to measure the antenna's azimuth), as soon as the system has received the return from an object, the computer must immediately read the antenna's azimuth for computing the coordinate of the object at the moment. Because of the delay in the course of tracking, a dynamic error is introduced to the system, and it affects the dynamic positioning precision of the radar. In this paper, a mathematical model describing the dynamic error is given. Based on this model, a method for testing the dynamic error is developed, which is easy to adopt from the engineering point of view. Also developed here is a new technique to improve the dynamic positioning precision by using a computer to correct the dynamic error. In conclusion, this paper gives the source program for correcting the dynamic error written in ALGOL-60, and the results of running the program on a NOVA machine.

AUTHOR: ZHANG Guoquan [1728 0948 2938]
NI Zhongkuang [0242 6850 0562]

ORG: ZHANG of Shanghai Wire Communication Factory; NI of the Department of Computer Science, Fudan University

TITLE: "Application of Kalman Filtering to Improving Accuracy of Radar"

SOURCE: Beijing DIANZI XUEBAO [ACTA ELECTRONICA SINICA] in Chinese No 3, 1981 pp 19-25

TEXT OF ENGLISH ABSTRACT: Kalman filtering can be used for target tracking, both in electronic scan radar systems and in mechanical scan radar systems. In the former systems it is used to directly initiate beams to move, while in the latter systems it is used for exact measurement without the problems caused by servo tracking structures. The tracking loop formed by Kalman filtering will have target bias-zero tracked when working in parallel with the servo-tracking loop. The state estimation of Kalman filtering serves as the coordinate output of radar measurement as well as the complex control signal for servo systems, thus realizing computer-aided-tracking. The video closing test shows that it performs satisfactorily.

In order to improve the accuracy and to solve the problems caused by the difference between model design and the actual moving of targets, this paper presents an adaptive method of detecting maneuvering by mean-variance and modifying gain directly. The flying tests of an experimental scan array radar show that this method is more effective than those without adaptive constant coefficient tracking systems.

AUTHOR: YANG Zhiyou [2799 5268 0645]

ORG: Xian Research Institute of Navigation

TITLE: "Compiling and Computing a New Type of Navigation Table"

SOURCE: Beijing DIANZI XUEBAO [ACTA ELECTRONICA SINICA] in Chinese No 3, 1981 pp 26-31

TEXT OF ENGLISH ABSTRACT: A new method of compiling and computing the hyperbolic lattice navigation tables is introduced. It is a new double argument navigation table with which the geodesic coordinates can be obtained directly from paired time differences. Its arrangement pattern and contents are completely from those of the present American LORAN table. The position fixing procedures are simplified. The geodesic coordinate of the receiver can be found simply by addition, subtraction and multiplication, and the predicted position of the vehicle need not be known. The troublesome drawing procedure also can be avoided. It takes only 1-2 minutes to make a position fixing by using this new table as compared with 3-5 minutes with the U.S. LORAN table.

AUTHOR: ZENG Lingru [2580 0109 0320]

ORG: Research Laboratory of Applied Physics, Chengdu Institute of Radio Engineering

TITLE: "Theoretical Analysis and Experimental Study of Double Y-Junction Circulator"

SOURCE: Beijing DIANZI XUEBAO [ACTA ELECTRONICA SINICA] in Chinese No 3, 1981 pp 32-36

TEXT OF ENGLISH ABSTRACT: The double Y-junction circulator is constructed by applying shunt open-circuited stubs to the center of a stripline simple junction. Its circuit model is established. The performance of its broad-band low VSWR is theoretically analyzed, and the design for a typical case is presented. A VSWR $\leqslant$ 1.10 and an isolation $\geqslant$ 26 dB are obtained in the 2.7 - 3.7 GHz range. The theoretical analysis coincides with experimental results very well.

AUTHOR: LIU Huizhong [0491 1920 0022]

ORG: Xian Institute of Radio Technology

TITLE: "Strip Polarizer and Strip-grid Polarizer"

SOURCE: Beijing DIANZI XUEBAO [ACTA ELECTRONICA SINICA] in Chinese No 3, 1981 pp 37-44

TEXT OF ENGLISH ABSTRACT: This paper gives two kinds of circular polarizers made of several photo-etched copper strips or strip-grid fiberglass epoxy plates. One is called the strip type, the other being the strip-grid type. The former performs well at center frequency, and the latter has broad-band performance. These two polarizers may be made into a polarized board as a cover set in front of the waveguide horn. Using curves and formulas given in the paper, the design and calculation may be very simple. Experiments have shown that within about 20 percent of the band-width of the strip type polarizer the axial ratio of the circular polarized field is better than 2 dB and VSWR is less than 1.1, and that within more than 20 percent of the band-width of the strip-grid type polarizer the axial ratio of the circular polarized field is better than 1 dB and VSWR is less than 1.1.

AUTHOR: WEN Junding [3306 0193 7844]

ORG: Research Institute No 724, Nanjing

TITLE: "A Generalization of Impedance Transformation Method for the Specific Waveguide"

SOURCE: Beijing DIANZI XUEBAO [ACTA ELECTRONICA SINICA] in Chinese No 3, 1981 pp 45-50

TEXT OF ENGLISH ABSTRACT: In this paper, the generalized impedance transformation method is used to solve the eigenequation and eigenvalue of the fundamental mode in the specific waveguide with various shapes. This method reduces the engineering calculation to solve the general equation. Its conciseness is very obvious, especially in dealing with complex problems. Several typical examples are computed and experimented with. The results of the computation are basically identical with those of Halford, Simmons and Lerner.

The specific waveguides have found many applications in microwave power sources and microwave magnetic devices. There have been a number of methods for analyzing and treating this kind of waveguide, but up to now no concise and general methods have been reported for dealing with various shape waveguides. The introduction of uncontinuous capacitances and the change of matrix elements which change with the variation of transverse impedances are considered, and by using the generalized

[Continuation of DIANZI XUEBAO No 3, 1981 pp 45-50]

impedances transformation method the eigenequation, which is, to a certain extent, general for various shape waveguides, is derived. This method can meet the requirements for engineering calculations.

AUTHOR: WANG Feng [3769 7685]
ZHANG Bingran [1728 3521 3544]
DOU Wenwei [4535 2429 5588]
et al.

ORG: All of the Research Institute of Electronic Materials, Fourth Ministry of Machine Building

TITLE: "Pure GaAs by Vapor Phase Epitaxy"

SOURCE: Beijing DIANZI XUEBAO [ACTA ELECTRONICA SINICA] in Chinese No 3, 1981 pp 51-55

TEXT OF ENGLISH ABSTRACT: In this paper the electro-parameters of high purity GaAs epitaxial layers and their process conditions are reported. The vapor epitaxial growth is obtained in the Ga-$AsCl_3$-H_2 reaction system at high water vapor partial pressure ($\approx 4.1 \times 10^{-5}$ atm) and low deposition temperature (650°C). The optimum mobility value at 77°K is 211,000 cm/s.V, and its corresponding peak (44.2°K) is 329,000 cm/s.V. The 77°K mobility values are generally repeated at 120,000-200,000 cm/s.V. The high purity materials have an outstanding characteristic of low compensative ratios. In this paper, the experimental results are briefly discussed.

AUTHOR: LONG Dehao [7893 1795 3185]

ORG: Department of Radio Electronics, Sichuan University

TITLE: "An Automatic Gain Control Circuit of Varying Time Constant"

SOURCE: Beijing DIANZI XUEBAO [ACTA ELECTRONICA SINICA] in Chinese No 3, 1981 pp 56-61

TEXT OF ENGLISH ABSTRACT: This paper presents an automatic gain control circuit in which the time constant varies continuously and automatically. Its physical process is first explained, and then its transient state and stable state are analyzed. Finally it is pointed out that the system is a generalization of the general automatic gain control circuit in which the time constant is fixed. Not only can the system suppress high level interference pulses and its output dynamic range, but it can also ensure a sufficiently low countermodulation distortion of useful signals at low levels.

An additional device is chiefly made up of the automatic gain control system of a varying time constant. Connecting the device with the terminal of the short wave receiving equipment EKV-12 (Berlin, 1975), it can lower the error code rate by 67 percent and raise the signal-noise ratio by 10 dB with respect to the EKV-12.

AUTHOR: LU Dakui [0712 1129 1145]

ORG: Shanghai Newlight Telecommunication Factory

TITLE: "A New Type of Frame Sync Code: Super-Barker-Code"

SOURCE: Beijing DIANZI XUEBAO [ACTA ELECTRONICA SINICA] in Chinese No 3, 1981 pp 62-69

TEXT OF ENGLISH ABSTRACT: This paper analyzes the probability of the false-frame sync and the number of false-frame syncs per frame in a digital transmission system. More exact equations for the number of false-frame syncs per frame are derived. It also provides the ideal curves that are different from traditional ones for determining the performance of the frame sync code. Based on this, a new type of frame sync code, the SB code (Super-Barker-Code), is recommended. When used as the frame sync code, its performance is superior to that of the Barker-Code.

AUTHOR: HE Guowei [0149 0948 0251]

ORG: Beijing Institute of Electromechanical Standardization

TITLE: "A Bayesian Approach for Estimating Increasing MTBF"

SOURCE: Beijing DIANZI XUEBAO [ACTA ELECTRONICA SINICA] in Chinese No 3, 1981 pp 70-74

TEXT OF ENGLISH ABSTRACT: The development of a complex electronic system may be divided into several stages. Let λ_1 be the failure rate of the system in the i-th stage. In many situations, the reliability of the system increases stage by stage, i.e., $\lambda_1 > \lambda_2 > \ldots > \lambda_m$. We choose the prior distributions of λ's to be $\pi(\lambda_1) \propto 1/\lambda_1$, such that the Bayes confidence interval of λ following the posterior density function is equivalent to the result of classical statistics. Let $f_1(\tau_1|\lambda_1)$ be the conditional probability function, where τ_1 is the total life time in the i-th stage. The posterior density function then is

$$f_m(\lambda_1, \lambda_2, \cdots, \lambda_m|\tau_1, \tau_2, \cdots, \tau_m) = \frac{\prod_{i=1}^{m} f_i(\tau_i|\lambda_i)\pi_i(\lambda_i)}{\int_0^{\infty}\cdots\int \prod_{i=1}^{m} f_i(\tau_i|\lambda_i)\pi_i(\lambda_i)d\lambda_1 d\lambda_2 \cdots d\lambda_m}$$

and the marginal posterior density function of λ_m is

$$f_m(\lambda_m) = \int_0^{\infty}\cdots\int f_m(\lambda_1, \lambda_2, \cdots, \lambda_m|\tau_1, \tau_2, \cdots, \tau_m)d\lambda_1 d\lambda_2 \cdots d\lambda_{m-1}$$

[Continuation of DIANZI XUEBAO No 3, 1981 pp 70-74]

where Θ is the space formed by $\Theta_1 \supset \Theta_2 \supset \Theta_3 \supset \ldots \Theta_m$, Θ_1 is the domain of λ_1, and Θ' is the subspace of Θ. The γ-confidence interval of λ_m is (o, λ_m^*), where

$$\int_0^{\lambda_m^*} f_m(\lambda_m)d\lambda_m = \gamma .$$

In classical statistics, we can only τ_m to calculate the γ-confidence interval for λ_m, because the statistics $\tau_i (i = 1, 2, \ldots, m-1)$ belong to another population. However, now we can use the formulas derived in this paper to calculate the γ-confidence interval for λ_m, not only by using τ_m, but also by using τ_1, τ_2, ..., τ_{m-1}. The size of the sample of the m-th stage using this method will be smaller than the sample of the m-th stage using the classical statistics method.

9717
CSO: 4009/391

AUTHOR: WANG Benxuan [3769 2609 6513]

ORG: Tianjin Municipal Research Institute of Radio Technology

TITLE: "The DJS132 Digital Computer, a New Computer of the DJS 100 Series"

SOURCE: Beijing DIANZI JISHU [ELECTRONIC TECHNOLOGY] in Chinese No 7, 81 pp 30-31

ABSTRACT: The DJS132 computer is based on China's highest production volume computer, the DJS130. It is a new type of computer which uses new technology and construction techniques. Its design emphasizes reliability, ease of use and maintenance, as well as amenability to high volume production and a limited number of components. It uses modular construction and fits into a 610 x 307 x 480 mm cabinet and is the smallest of China's comparable computers. It retains the rich and complete software of the DSJ130 and uses the Single Operating System (SOS) and the Real-time Operating System (RTOS), the Real-time Disk Operating System (RDOS,) depending upon the speed and complexity of the peripheral operations. All languages can be used under RDOS, including FORTRAN IV, ALGOL 60, and BASIC.

AUTHOR: NIU Lin [3662 7207]

ORG: Beijing Computer Plant No 3

TITLE: "Improvements to the DJS140 Computer System"

SOURCE: Beijing DIANZI JISHU [ELECTRONIC TECHNOLOGY] in Chinese No 7, 81 p 32

ABSTRACT: The DJS140 computer system is an improvement over the 100 system. Its design was firmed up in Aug 79. A prototype was produced after one year of efforts. The system hardware includes the central processor, the floating point processor, and the storage protect feature. The cpu has hardware multiply/divide. The internal memory has 64 K words expandable to 128 k. It has a memory cycle time of 1.1 - 1.4 μsec. Peripherals include the real-time clock, plotter, disk, and half inch tape drives. System software includes the MRDOS operating system, and FORTRAN, ALGOL, and BASIC languages. The 140 features increased reliability and improved coordination and serialization.

6168
CSO: 4009/440

AUTHOR: ZHANG Lixin [1728 4539 2450]
LUO Jixun [4382 4949 0534]
YIN Yaode [6892 5069 1795]
et al.

ORG: All of the Institute of Metal Research, Chinese Academy of Sciences

TITLE: "Effects of Rare Earth on Preferred Orientation in Oxide Scale of a Fe-Cr-Al Alloy"

SOURCE: Beijing JINSHU XUEBAO [ACTA METALLURGICA SINICA] in Chinese No 3, 1981 pp 233-242

TEXT OF ENGLISH ABSTRACT: The effects of RE additions, 0.5 percent Y or 0.15 percent (La + Ce), on the preferred orientation of oxide scale formed at 1200°C in an Fe-Cr-Al alloy have been studied by the inverse-pole-figure method. It was found that the addition of RE elements affects the types of preferred orientation to a limited extent. The main preferred orientation in the oxide scale on three tested alloys are identical as $(01\bar{1}8)_{\perp}$; whereas some differences are shown among their minor ones with $(11\bar{2}9)_{\perp}$ and $(10\bar{1}10)_{\perp}$ for alloys containing Y or La + Ce, and $(0001)_{\perp}$ and $(10\bar{1}10)_{\perp}$ for an alloy without RE. RE can play an important part in conserving and enhancing the preferred orientations in the scale, of which Y has a more remarkable effect than does La + Ce.

[Continuation of JINSHU XUEBAO No 3, 1981 pp 233-242]

The oxidation process of the alloys was described by the short circuit dislocation path model. This model makes the variation curve of $P_{10\bar{1}1}$ parameter of the oxide scale in good agreement with the variation curves of oxidation dynamics. This accounts for the fact that RE elements improve the oxidation resistance of the alloy through their effect on modifying the preferred orientation of the oxide scale.

AUTHOR: LUO Yang [5012 7122]
LI Weili [2621 0251 4539]
LI Yufeng [2621 3768 7685]
et al.

ORG: All of the Central Iron and Steel Research Institute, Ministry of Metallurgical Industry

TITLE: "Effect of Al on the Magnetic Properties of Grain-oriented 3 Percent Si-Fe"

SOURCE: Beijing JINSHU XUEBAO [ACTA METALLURGICA SINICA] in Chinese No 3, 1981 pp 243-252

TEXT OF ENGLISH ABSTRACT: Studies were made of the effect of Al on the magnetic properties of grain-oriented 3 percent Si-Fe containing about 0.007 wt-percent N and 0.001 - 0.0088 wt-percent Al. The nitrogen content, both soluted and combined in steels, was determined by the hydrogen extracting method. It is shown that every optimum range of Al content in steels is available to its own soaking temperature for the purpose of obtaining proper magnetic properties as $B_{10} \geq 1.8$ T and $P15/50 \leq 1.05$ W/kg, such as 0.008 - 0.018, 0.005 - 0.022, 0.004 - 0.03 and 0.05 wt-percent Al which correspond to 1200, 1250, 1300 and 1350°C respectively. If any Al content was beyond the optimum range, its magnetic properties would fall steeply to the same extent as that of the value of the non-oriented steel. It is also found that the Al content influences markedly the proportion of AlN which is an effective inhibitor

[Continuation of JINSHU XUEBAO No 3, 1981 pp 243-252]

to normal grain growth. Most effective AlN may be precipitated when the acid soluble Al is within 0.005 - 0.02 percent. Due to the aforementioned results, together with those of electron microscope observation and thermodynamical consideration of AlN and MnS, an approach to the behavior of Al on magnetic properties of grain-oriented 3 percent Si-Fe was proposed, namely, the Al is associated with N to form AlN, and then AlN exists as an effective inhibitor.

AUTHOR: LONG Qiwei [7893 2601 1218]

ORG: Institute of Metal Research, Chinese Academy of Sciences

TITLE: "Relationship between Mechanical Property of Metals and Critical Fracture Angle of a Slanted Crack"

SOURCE: Beijing JINSHU XUEBAO [ACTA METALLURGICA SINICA] in Chinese No 3, 1981 pp 253-258

TEXT OF ENGLISH ABSTRACT: A new concept of two critical angles was suggested for fracture analysis of a slanted crack. A discussion was particularly made of the material choice for small slant angle experiments. It is shown that all the metallic materials which used to be conventionally employed in such experiments seem to not be the most satisfactory ones.

AUTHOR: YIN Jiang [3009 0561]
XU Jingfeng [6079 4842 1496]

ORG: Both of the Shanghai No 5 Steel Works

TITLE: "Fracture Mechanics Analysis of Cold-drawn Si-Cr Valve Steel"

SOURCE: Beijing JINSHU XUEBAO [ACTA METALLURGICA SINICA] in Chinese No 3, 1981 pp 259-265

TEXT OF ENGLISH ABSTRACT: A fracture mechanics approach was used in studying the cold-drawn splitting in Si-Cr valve steel. It seems that the cold deformation fracture toughness, K_{Ic}, the peak value of cold-drawn tangential residual tensile stress, σ_{tm}, and the depth of surface blemish, a, are the three main factors affecting the splitting. An expression to determine the growth of splits in cold-drawn rods may be as follows:

$$K_{Ic} = \sigma_{tm}(\pi a)^{1/2}(K_I/K_0).$$

The exact value of K_{Ic} is easily given by a cold-heading specimen after cold deformation. Thus, the cold-drawing process makes it possible to control the blemish depth. This process allows the steel to withstand a single cold drawing reduction of 20-30 percent or more at room temperature without splitting or recrystallizing the granular fracture and to give a superior performance that could not be obtained previously by hot drawing.

AUTHOR: ZHANG Jushui [1728 5468 3055]

ORG: Research Institute of Daye Steel Works

TITLE: "Lamellar Fracture Characteristics of Medium-carbon CrNiMoV Steel Forgings"

SOURCE: Beijing JINSHU XUEBAO [ACTA METALLURGICA SINICA] in Chinese No 3, 1981 pp 266-270

TEXT OF ENGLISH ABSTRACT: The lamellar fracture with streaky matt facets found in the cracked surface of medium-carbon CrNiMoV steel forgings has been observed by TEM. Various extracted second phases in carbon replicas from the fracture surface were identified by selected-area electron diffraction technique and EPMA. The results indicate that the fine globular α-MnS, type-I MnS inclusion and thin platelet or dentritic VC appeared, as well as the flaky complex oxides of Si and Mn, mainly as SiO_2, distributed along the direction of hot forging. The lamellar fracture characteristics relating to intercrystalline cracking are due to various second phase precipitates at the primary austenite grain boundaries. It seems that the lamellar fracture is similar to the "rocky-rock candy" one in cast steel substantially, thus it may decrease remarkably the transverse tensile ductility and lower moderately the impact toughness of the steel.

AUTHOR: ZHANG Zhenfang [1728 2182 5364]
ZHANG Tianyi [1728 1131 1355]
LIU Minzhi [0491 0046 3112]

ORG: All of the Institute of Metal Research, Chinese Academy of Sciences

TITLE: "Correlation between Numeral Fracture Characteristics and Fracture Toughness of Medium-carbon CrNiMo Steel"

SOURCE: Beijing JINSHU XUEBAO [ACTA METALLURGICA SINICA] in Chinese No 3, 1981 pp 271-277

TEXT OF ENGLISH ABSTRACT: An investigation was conducted to observe the microstructure and macro- or micro-fracture surface, and to determine the fracture toughness and impact toughness of fatigue precracked specimens of four different types of structure of a medium-carbon CrNiMo steel. Some primary results indicated that its highest fracture toughness was evaluated by specimens of sorbitic structure tempered at 600°C, but the lowest were at 300°C. An identical variation is noted between the impact toughness of the fatigue precracked specimens and the fracture toughness from tri-point bending tests. Moreover, the numerical estimation for the various fractured surface characteristics in relation to fracture toughness has been attempted.

AUTHOR: NING Yuantao [1380 6678 3447]
ZHOU Xinming [0719 2450 6900]

ORG: Both of the Institute of Precious Metals Research

TITLE: "A Criterion of the Formation of Amorphous State by Melt Quenching"

SOURCE: Beijing JINSHU XUEBAO [ACTA METALLURGICA SINICA] in Chinese No 3, 1981 pp 278-284

TEXT OF ENGLISH ABSTRACT: A criterion of the formation of amorphous state alloys by melt quenching has been proposed as $I/\Delta S < 0.032$ and $(I - 0.1)/\Delta S > 0.0044$, where $I = 1 - T_m/\bar{T}_m$ and $S = \frac{1}{100C_B}(\bar{T}_m - T_m)$, T_m = melting point of the alloy, $\bar{T}_m$ = weighted average melting points of its components and C_B = at percent of solute B. However, this criterion seems to be more accurate since special account has been taken of the effects of alloy composition and intermediate phases. All 127 alloys, with only one exception, checked well with the criterion. Furthermore, the concentration distribution of the amorphous alloys and the characteristics of the allied constitution diagrams have been discussed.

AUTHOR: ZHANG Bangwei [1728 6721 4850]

ORG: Hunan University

TITLE: "Effect of Size Factors on the Formation of Amorphous Alloys"

SOURCE: Beijing JINSHU XUEBAO [ACTA METALLURGICA SINICA] in Chinese No 3, 1981 pp 285-292

TEXT OF ENGLISH ABSTRACT: An attempt was made to approach the general law of the amorphous alloy formation. From the previous available experimental data, it is proposed that half of the tested inter-atomic distance, instead of the atomic radius of the constituent elements, taken as a measure for predicting the formation of amorphous alloys seems to be more satisfactory. The size factor $\Delta R/R_1$ of the constituents which form the binary or multiple amorphous alloys is usually greater than 9 percent with only a few exceptions. For a binary alloy, the expression which represents the condition necessary for its formation may be given as:

$$\left|\left(\frac{Z}{r_A}\right)_B (\delta x_B)_A (x_{B,A} - x_{B,B})\frac{\Delta R}{R_1}\right| \geq 0.09$$

About 90 percent of the alloys formed by splat quenching from their melts fulfill the expression.

AUTHOR: JI Jingwen [2061A 2529 2429]
LI Maohua [2621 5399 5478]
XIAO Lianfang [5135 6647 5364]
et al.

ORG: All of the Baotou Institute of Metallurgy

TITLE: "Experimental Studies on Low Temperature Brittleness of Phosphorus Containing Steels and Iron-phosphorus Alloys"

SOURCE: Beijing JINSHU XUEBAO [ACTA METALLURGICA SINICA] in Chinese No 3, 1981 pp 293-299

TEXT OF ENGLISH ABSTRACT: A fractographic study of 10MnP and 15MnP steels with or without RE additions, as well as on iron-phosphorus alloys under normalized or annealed and then reheated at 700°C WC conditions has been carried out by SEM. The electrode potentials on the fracture or polished surface of the RE free steels have been determined, and further investigations on their fractures have also been made by AES and ion-probe analysis. It was found that no intergranular fracture occurs in any of the specimens ruptured at room temperature to -100°C. Most of the fractures are brittle cleavage in nature, except that a little ductile fracture appeared on fractures of the specimens ruptured at the interval from room temperature to -25°C. It seems that the cleavage fractures are enriched with phosphorus.

AUTHOR: ZHANG Qiyun [1728 0796 6663]
LIU Shuqi [0491 3219 4388]

ORG: Both of the Department of Chemistry, Beijing University

TITLE: "Selection of Filler Metal for Aluminum Brazing and Its Reaction with Base Metal"

SOURCE: Beijing JINSHU XUEBAO [ACTA METALLURGICA SINICA] in Chinese No 3, 1981 pp 300-306

TEXT OF ENGLISH ABSTRACT: The influence of 28 element additions on the melting point, flowability, corrosion resistance and fillet bending ability of Al-Si type filler metal has been investigated. Among these systems, filler 6M, i.e., Al-Si (13.0)-Be (0.4-0.8)-Sr (0.03-0.06)-La (0.03-0.06), is regarded as the optimum. The erosion mechanism of molten filler metal on base metal has also been studied. In addition to the influences of brazing temperature and the composition of filler metal, the rate of solution of base metal into molten filler and the spreading out of molten filler along the fillet are also of importance in affecting the erosion of base metal during brazing. The fillets were annealed for different time intervals and only a small improvement of their strength and bending capacity was observed.

AUTHOR: ZHANG Yonggang
et al.

ORG: None

TITLE: "Change of Carbon Contamination During Uranium Refining"

SOURCE: Beijing JINSHU XUEBAO [ACTA METALLURGICA SINICA] in Chinese No 3, 1981 pp 352-354

TEXT OF ENGLISH ABSTRACT: An investigation was undertaken to obtain a better understanding of the increase of carbon contamination in uranium during refining with graphite crucible. The results indicate that the increasing rate of carbon content, c, in uranium melt with respect to refining time, t, may be proposed as:

$$\frac{dc}{dt} = ks(1 - \frac{c}{c_s}),$$

where k is a constant, s is the specific contact surface between melt and graphite crucible, and c_s is the solubility of carbon in uranium melt.

AUTHOR: YANG Yingchang [2799 2019 2490]

ORG: Department of Physics, Beijing University

TITLE: "Structural and Magnetic Properties of $Y(Mn_{1-x}Fe_x)_{12}$"

SOURCE: Beijing JINSHU XUEBAO [ACTA METALLURGICA SINICA] in Chinese No 3, 1981 pp 355-358

TEXT OF ENGLISH ABSTRACT: The new ternary intermetallic compounds on the iron-rich side, $Y(Mn_{1-x}Fe_x)_{12}$ have been prepared and their magnetic properties investigated. Their structure was found to be of the $ThMn_{12}$ type with x = 0.8 after appropriate annealing. The field dependence of magnetization was measured under the range of 4.2 K to room temperature. The results indicate that $Y(Mn_{1-x}Fe_x)_{12}$ appears antiferromagnetic when x = 0.0, 0.2 or 0.4, in a spontaneous magnetization when x = 0.6, and to become ferromagnetic or ferri magnetic when x = 0.8. The Curie point is above room temperature.

9717
CSO: 4009/363

END

END OF FICHE

DATE FILMED

11 SEPT 1981